

Article

Digital Field Mapping and Drone-Aided Survey for Structural Geological Data Collection and Seismic Hazard Assessment: Case of the 2016 Central Italy Earthquakes

Daniele Cirillo ^{1,2} 

¹ Dipartimento di Scienze Psicologiche, della Salute e del Territorio, Università G. d'Annunzio, via dei Vestini 31, 66100 Chieti, Italy; d.cirillo@unich.it; Tel.: +39-0871-355-6389

² Centro InterUniversitario per l'Analisi SismoTettonica tridimensionale (CRUST), Italy

Received: 14 June 2020; Accepted: 26 July 2020; Published: 29 July 2020



Abstract: In this work, a high-resolution survey of the coseismic ground ruptures due to the 2016 Central Italy seismic sequence, performed through a dedicated software installed on a digital device, is strengthened by the analysis of a set of drone-acquired images. We applied this integrated approach to two active sections of the Mt Vettore active fault segment which, in the Castelluccio di Norcia plain (central Italy), were affected by surface faulting after the most energetic events of the sequence: the 24 August, Mw 6.0, Amatrice and 30 October, Mw 6.5, Norcia earthquakes. The main aim is to establish the range in which the results obtained measuring the same structures using different tools vary. An operating procedure, which can be helpful to map extensive sets of coseismic ground ruptures especially where the latter affects wide, poorly accessible, or dangerous areas, is also proposed. We compared datasets collected through different technologies, including faults attitude, dip-angles, coseismic displacements, and slip vectors. After assessing the accuracy of the results, even at centimetric resolutions, we conclude that the structural dataset obtained through remote sensing techniques shows a high degree of reliability.

Keywords: drone-acquired imagery; high-resolution topography; digital mapping; compass-clinometer integrated tablet; coseismic ruptures; aero photogrammetry; 2016 Central Italy seismic sequence; virtual outcrop; structure-from-motion

1. Introduction

The new technologies that replace 20th-century field tools are the smartphone, handheld Global Navigation Satellite System (GNSS), tablets, iPad, and drones. Last generation tablets, in particular, offer performances of a hand-compass, plus take pictures and act as both a notebook and mapping device, and gather precise location data using GNSS. They can even be equipped with GIS software. The impressive technological development characterizing the current times have also brought significant improvement in field mapping techniques. The “classical” geological survey can now be integrated by digital mapping carried out using several types of devices, like tablets with dedicated software, and in some particular contexts, by the acquisition of images by drones [1–14]. This work provides a workflow for drone remote-sensing and structural-geological mapping, which offer significant advantages compared to the traditional fieldwork. The collected data enable us to reconstruct three-dimensional models of inaccessible outcrops and to explore in detail areas which, during a repetitive seismic activity, might be affected by rock falls (cliffs or outcrops at the foot of prominent fault scarp).

Furthermore, compared to the traditional methods that employ compass-clinometer and field book, digital mapping, performed either with tablets and/or drones, allow collecting an enormously

greater number of data, thanks to the fast and continuous acquisition procedure and the automatic georeferencing. As an example, more than 4000 survey data, as type of rupture, attitude, kinematics, slip vector (obtained from coseismic slickenlines or piercing points), and displacement (throw, opening, and net displacement) were acquired along the Mt Vettore-Mt Bove Fault (VBF) over a total length of about 30 km, immediately after the two major seismic events. The survey was performed at a high resolution, with a sampling rate of at least one site per 50 m, and locally of three sites per meter. All data reported and discussed in Brozzetti et al. [15] has been collected through the Fieldmove app installed on iPad dispositive. During the aforementioned survey, the traditional mapping methods were supported by digital technologies, such as digital field mapping and drone-aided survey, which turned out to be useful to sensibly reduce the working time and to collect such massive field datasets.

Furthermore, the use of multiple work tools, even on the same site, has allowed us to compare the effectiveness of the various applied methods and, at the same time, making cross-checks to test their reliability.

Here, we report on the results of the high-resolution structural mapping of the coseismic ground deformations due to surface faulting that followed the strongest events of the 2016 Central Italy seismic sequence, which are the August 24, Mw 6.0, Amatrice; and the October 30, Mw 6.5, Norcia earthquakes.

In this work, we explored the advantage, conditions of applicability, and limits of the proposed novel approach to map and parameterize the coseismic ruptures, hundreds of meters or kilometers long, occurring along two synthetic splays of the VBF herein referred to as Colli Alti e Bassi (CAB) and Prate Pala (PTP) faults. The CAB had been known for a long time in published geological maps, thanks to its excellent surface exposure; the second was unveiled by recent paleoseismological research [16], which highlighted at least three reactivations during the Holocene.

Along these faults, where a detailed survey of coseismic ruptures was available [15], the quality of the results here obtained through high-resolution aerial photogrammetric images acquired using a small-size low-cost drone, has been tested and discussed.

1.1. Study Area

The study areas are located near the village of Castelluccio di Norcia ($42^{\circ}49'42.51''$ N $13^{\circ}12'28.00''$ E) in the southern part of the Sibillini Mts. chain, a deeply studied portion of the Umbria-Marche thrust and fold belt in Central Italy [17–19]. The stratigraphy of this region includes a Jurassic-Middle Miocene, shelf to pelagic, carbonatic succession, followed upward by Late Miocene siliciclastic turbidites (Figure 1).

The contractional structures consist of a system of NW-SE to N-S-striking asymmetric box-folds characterized by overturned eastern limbs and bounded by east-verging low-angle thrust faults, Late Miocene-Early Pliocene in age [18,20,21].

Towards E and SE, the outer basal thrust of the chain which, from N-S direction, turns southwards to NNE-SSW direction, causes the superposition of the Sibillini thrust sheet on the Messinian Laga basin turbidites.

Since the Early Pleistocene, extensional fault systems displaced the contractional structures [22–24] with associated offset, along the single faults, locally exceeding 1500 m. Despite the fault system showing a certain geometrical complexity, on the whole, the Quaternary normal faults appear arranged in a quite a regular, NNW-SSE-striking regional alignment across the Umbria-Marche and Laga domains (Figure 1a).

During the Quaternary, the activity along the major extensional faults, which dip to W-SW, led to the formation of intra-mountain basins, filled with alluvial and lacustrine deposits [25–27].

The easternmost extensional fault, the VBF, is a highly segmented, well-known active structure with a $6.5 \leq Mw \leq 6.8$ maximum expected magnitude [28] (Figure 1a). It shows an along-strike length of ~30 km, a long-term maximum displacement of ~1500 m [21,25,29], and a maximum Late Quaternary slip rate of 1.3 mm/y [15].

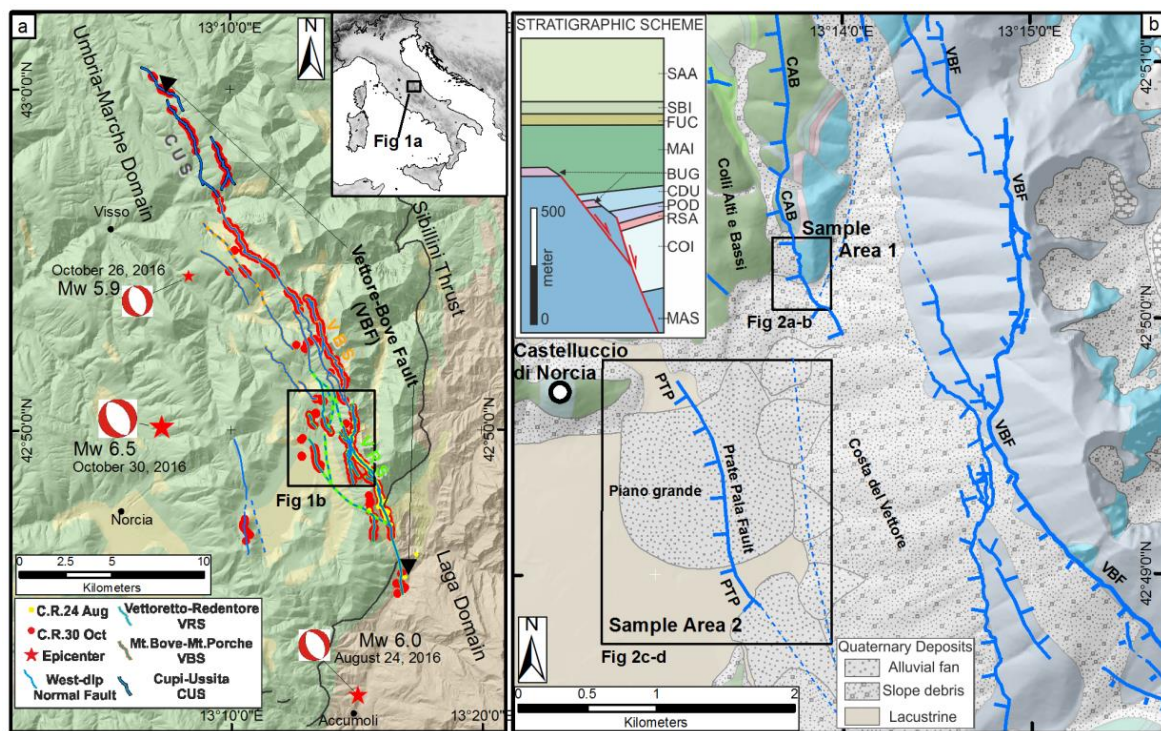


Figure 1. ((a)—top-right inset): location map of the study area in the central Apennines of Italy; ((a)—main figure) Structural sketch of the Mt Vettore-Mt Bove fault (VBF), with epicenters (red stars) and focal mechanism of the three $M > 5.5$ earthquakes of the 2016 seismic sequence, <http://terremoti.ingv.it/>; Geological key color—green: Umbria-Marche Domain, brown: Laga Domain, yellow: Quaternary deposits; (b) Geological map of the study area, after Pierantoni et al. [29], modified, and location map of the two sample areas (1 and 2) where the Colli Alti e Bassi (CAB) and e Prate Pala (PTP) splays of the VBF crop out; top-left inset shows the stratigraphic scheme of the area extracted from Pierantoni et al. [29]; MAS: Calcare Massiccio; BUG: Bugarone Group; COI: Corniola; RSA: Rosso Ammonitico; POD: Calcarei a Posidonia; CDU: Calcarei Diasprigni; MAI: Maiolica; FUC: Marne Fucoidi; SBI: Scaglia Bianca; SAA: Scaglia Rossa.

The Piano Grande basin was developed in the VBF hanging wall during the Middle-Late Pleistocene (Figure 1b). Eluvial-colluvial deposits overlay unconformably the carbonate bedrock along the borders of the basin whereas the major depression is mainly filled by alluvial and lacustrine sediments [30,31].

Well before the 2016 Central Italy seismic sequence, the present activity of VBF had been suggested on the base of the observed displacement of Quaternary deposits and Late Pleistocene—Holocene landforms [21,23,25]; subsequently its seismogenic potential was highlighted by paleoseismological evidence [28].

The diffuse surface faulting observed along the VBF after the 2016 sequence (Figure 1b) and the good correlation between the activated fault at the surface and the hypocentral distribution of the seismicity unquestionably confirmed the seismogenic role of this fault.

All the three main segments in which the VBF is divided were activated during the 2016 seismic sequence; they are referred to, from south to north, as the Vettoretto-Redentore, Bove-Porche and Cupi-Ussita segments [15] (Figure 1a).

Several synthetic and antithetic splays branch from the three segments at distance up to 4 km west of the main fault trace.

Two of the major splays of the Vettoretto-Redentore segment, located along the eastern border of the Piano Grande di Castelluccio basin, and named hereinafter the Colli Alti e Bassi Fault and Prate Pala fault (CAB and PTP, respectively, Figure 1b) were affected by significant coseismic reactivation and have been studied in detail in this work.

1.2. Distribution of the Coseismic Ruptures

The 24 August, M_w 6.0, Amatrice earthquake [32,33] caused the reactivation of the Vettoretto-Redentore segment of the VBF VRS, (Figure 1a,b), [15,34,35]. The 26 October (M_w 5.4 and M_w 5.9) and 30 October (M_w 6.5) events continued the reactivation of the VBF causing respectively the rupturing of its northern (Cupi-Ussita) and central (Bove-Porche) segments and reactivating again the Vettoretto-Redentore segment.

Massive field surveys performed by several research groups after the three earthquakes, allowed to reconstruct and compile very detailed databases of the associated primary ruptures [15,36–38] (yellow and red dots in Figure 1a).

To date, most authors [15,39–41] agree that: (i) the M_w 6.0 event caused surface faulting, along a ~ 6 km section of the VRS, with coseismic throws reaching 27 cm, without activating any other splay of VBF; (ii) the 26 October M_w 5.9 event ruptured the only northern segment of the VBF, (Cupi-Ussita), with throws ranging from 8 to 10 cm; (iii) the 30 October (M_w 6.5) mainshock reactivated and ruptured the entire Vettoretto-Redentore and Bove-Porche segment, with a surface rupture length $32 > L > 22$ km and coseismic surface displacements up to 222 cm, and (iv) despite most of the 30 October coseismic ruptures having occurred along the main fault trace, they also partially reactivated synthetic and antithetic splays within a few kilometers off the main fault trace. On the contrary, no evidence of coseismic rupture was observed after the 24 August event along the subsidiary structures.

1.3. Selection of Sample Areas

In the Castelluccio di Norcia area (Figure 1b), two cases of significant coseismic fault-reactivation occurred, after the 30 October mainshock, along the Colli Alti e Bassi (CAB) [(42°50'10.06" N 13°13'46.35" E)] and Prate Pala (PTP) [(42°49'10.70" N 13°13'23.15" E)] normal fault (Figure 2a,b). The CAB geologic (i.e., long term) expression was previously recognized and reported in published geological maps [21,29].

The PTP was recognized and partially mapped by Galadini and Galli [16] through an aerial photo-geologic survey, integrated by paleoseismological trenching.

Both these reactivated synthetic splays of the VRS crop out close to the eastern border of the Piano Grande basin. We selected the sample area 1, straddling the CAB, and the sample area 2, including the PTP ruptured during the 2016 mainshock (Figure 2a,b).

In neither area, evidence of ruptures were detected after 24 August and 26 October events (Figure 3a,b,e); thus, the total measured displacements can be referred to the 30 October reactivation.

Digital fieldwork carried out on both the sample areas soon after the mainshock provided coseismic displacement values of up to 101 cm along the CAB (Figure 3c,d) and of 14 cm in the central part of the PTP (Figure 3f–h).

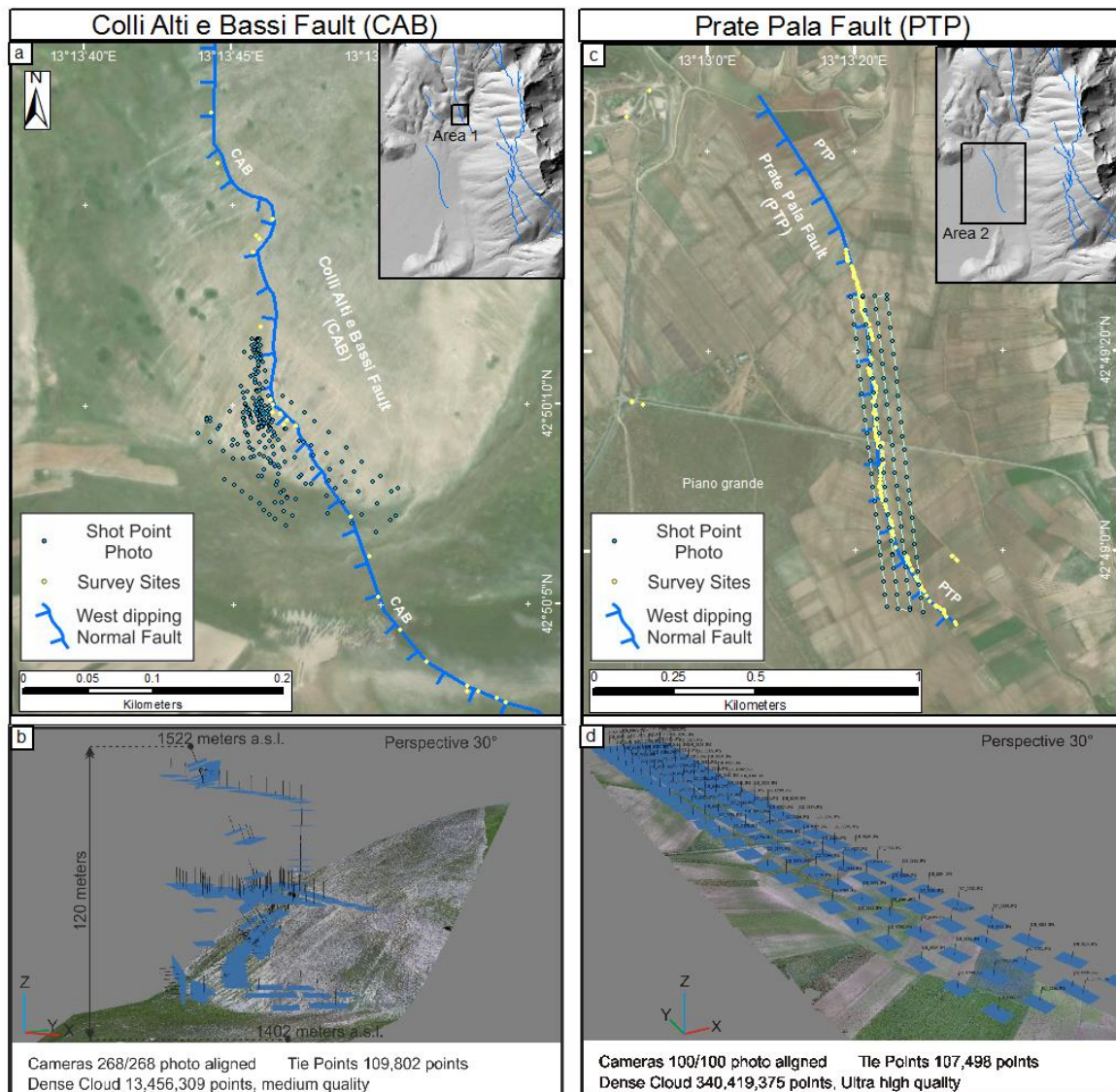


Figure 2. (a,b) Sample area 1, along the Colli Alti e Bassi Fault (CAB, location in Figure 1b); the two sketches (a = plan view, b = bird's eye view) illustrates the mission flight plan for image capturing over the sample area using a manual flight, with an overlap of 80% along the path and 80% in a lateral direction, useful to have a good alignment of images and to reduce the distortions on the resulting orthomosaics; (c,d) Sample area 2, along the Prate Pala Fault; (PTP, location in Figure 1b) the two sketches (c = plan view, d = bird's eye view) illustrates the mission flight plan for image capturing that covers the area using north-south flight paths with 65% along the path and 60% in a lateral direction. Legend: blue point: shot point photo; yellow point: sites of manual and digital mapping; blue line: trace of the CAB (a) and PTP (b) faults; tics indicates the hanging wall block.



Figure 3. (a–d): Sample area 1—the same outcrop of the CAB fault scarp shot at three temporal stages: (a) before the beginning of the 2016 seismic sequence, (b) after the 24 August and 26 October events but before the 30 October one, and (c,d) after the 30 October mainshock (bottom left on each image, date and the hour of photo shooting); (e–h): sample area 2—images at different scales, of the coseismic surface effects of the 30 October mainshock along the PTP fault trace.

2. Materials and Methods

2.1. Field Mapping

The high-resolution mapping of the surface coseismic ruptures in the field was carried out integrating the traditional survey, performed using a geologic compass-clinometer for measurement of planar and linear elements (dip azimuth/ dip-angle of fault planes, trend and plunge of slickenlines), with digital mapping technique. The digital mapping was based on a digital compass-clinometer App

for portable devices, allowing the direct measurement of georeferenced planar and linear elements accompanied by written notes, sketches, and editable photographs of each survey site (Figure 4). The “Fieldmove” App for smartphones, tablets, and iPad, developed by Midland Valley & Petroleum Experts [42], Glasgow-Edinburgh Scotland, was chosen and installed on an Apple iPad Air2 wifi-cellular (128 GB memory) with an internal A-GPS GLONASS/GNSS.



Figure 4. Survey tools used during different fieldwork activities: above: Traditional compass-clinometer and Digital device (Apple iPad Air2) supporting the “Fieldmove” App by Midland Valley & Petroleum Expert, in position for the measurement of a shear plane within a fault breccia; below: Drone model DJI Phantom 3 Professional and details of its components; Sony camera DSC-HX5V with integrated GPS; bottom-right: traditional papery field book.

Several preliminary trials allowed to verify that the internal sensor of IOS provides reliable and precise azimuthal and dip-angle measures. The reliability-trials consisted of repeated comparisons between measures of the same structure carried out using the digital device and the geological compass-clinometer. This testing experience highlighted that the chosen device and software assured accurate compass readings for both azimuthal and clinometric measurements that not exceed ± 2 degrees. For the positioning of the elements measured, an internal sensor A-GPS and GLONASS/GNSS also integrated with the high-resolution images from the Google Earth™ Pro 7.3 was successfully used. The accuracy of the waypoints acquired depended on satellite coverage. When the maximum satellite coverage reached the optimum values, the error estimated for the automatic location was of 1–2 m, whereas it reached 3–5 m in the worst coverage conditions. The solution to minimize the error location (well below one-meter resolution) was the manual adjusting on the iPad screen, taking into account the easily recognizable elements on the Google Earth base map imagery. A further precaution to avoid positioning inaccuracies was the use, as Fieldmove base maps, of previously acquired high-resolution images, orthorectified through ArcGis, and exported from the Move software in mbtiles or geotiff format file.

Field data were organized in a comprehensive GIS-managed dataset for subsequent elaborations. The used software aside from the Fieldmove App for Apple iPad includes Esri ArcMap 10.x and Move 2019 Petex suite [<http://www.petex.com/products/move-suite/>]. All the geological-structural data acquired were elaborated within the Move suite software Petroleum Experts see Section 3.1.2.

2.2. Georeferenced Field Images Dataset

The database of georeferenced images also used for reconstructing virtual outcrops includes the photographs shot during the digital survey, using the Fieldmove dedicated tool, and hundreds of digital photographs taken through a compact Sony camera with an integrated GPS sensor. Furthermore, it has been improved by several sets of high-resolution aerial photographs acquired through a digital camera transported by a Drone (Figure 4), whose methods of acquisition and processing is reported in the following Section 2.3.

Photogrammetric processing led to elaborate two Digital Surface Models (DSM) at centimetric resolutions for both the study-cases.

For their processing, different software as Agisoft Metashape Professional [<https://www.agisoft.com/>], Cloud Compare [<https://www.danielgm.net/cc/>], Esri ArcMap v.10.x, Move 2019 Petex suite [<http://www.petex.com/products/move-suite/>] were used.

2.3. Remotely Acquired Images and Data

2.3.1. Instruments Calibration and Pre-Drone Survey

The use of cameras for the Structure From Motion (SfM) and the creation of tri-dimensional virtual outcrops is now straightforward and fast because the instrumentation at our disposition is very light to transport during the field survey.

The necessity of total stations GPS for the acquisition of more precise and more accurate data positioning is generally required, but in this work, we did not use it. The method used in this research is based mainly on the placement of markers Ground Control Points (mGCPs) at a well-defined known distance during the field survey. The objectives of this work do not take into account the accuracy in terms of positioning of the virtual outcrop in the space (that is in terms of absolute coordinates), but it aims at achieving high-precision in the measurement of the outcrops parameters, as f.i. height of slopes, width, and length of the virtual outcrop, amount of coseismic displacement associated with each part of the rupture. Therefore, this research proposes a method of utilizing photogrammetry for creating a georeferenced and scaled virtual outcrop without the use of total stations GPS. The method is based on the use of an mGCPs of known geometries located close to outcrop during the field survey. The markers located on outcrops are used as ground control points, and their distances are calculated.

The acquisitions of mGCPs are essential in the pre and post-processing phase, to make scale changes, to position, orientate, and rescale the three-dimensional model in the chosen Geographic Reference System. In this work, 25 × 25 cm markers were used as mGCPs.

During the subsequent analysis through the Agisoft Metashape software, the placement of markers were positioned at the center of each mGCPs surveyed, to optimize precision between the images, and for subsequent rescaling of the virtual outcrop. The contrasting black and yellow rectangles of mGCPs, allow easily recognizable common points on each acquired photo and also facilitate the automatic location of points belonging to different images.

To improve the reliability of the measurement performed on a virtual outcrop, different calibers oriented in the third dimension (zy/zx plane = height, yx plane = width and length), perpendicular to each other were added.

The caliber instruments as hand-ruler 25 m long, aluminum stadia graduated rod 5 m long, and markers positioned at predetermined distances were used.

This method provided good precision in evaluating the virtual outcrop parameters, but it does not take into account the absolute accuracy in terms of geographical positioning; therefore, the whole model could also be shifted by some decimeters. In this work, all the markers were positioned at a distance of 10 m from each other and arranged in two preferential orthogonal directions North-South and West-East.

In the sample area 1, they were positioned at the intersection points of a 10 m sided square grid oriented in N-S and W-E directions (Figures 1b and 2a,b). Overall, in this area, 15 mGCPs, 7 of which

in the fault footwall and 8 in the hanging wall, and different calibers were used for scaling the entire model proportionally in both the directions N-S and W-E of the obtained virtual outcrop model.

The area 2, characterized by a narrow and elongated shape (1×0.13 km), to reduce the 'doming' effect [eg 10, 12, 13], a total of 20 mGCPs were arranged in the fault footwall, in the hanging wall, and also at corners and central part of the investigated area (Figures 1b and 2c,d).

2.3.2. Drone Survey

The aircraft used to perform the survey was a quadcopter. The drone is equipped with an autopilot package that, in the presence of internet connection, follows a pre-programmed flight-path using the appropriate app, enabling the user to choose the number of waypoints, the photo shooting, and the desired flight altitude. The mission program for both the study areas included a detailed flight plan, including the flight direction, number of flight lines, flying altitude, and orientation of the camera respect to the flight path. The program was thought taking into account that the awaited resolution of the post-processing images strongly depends on the overlap, side lap, and ground sampling distance.

A drone camera with sensor 1/2.3" CMOS, 12.4 M Effective pixels, lens FOV 94° 20 mm (35 mm format equivalent), image size of 4000×3000 was used for the survey; for more detailed resolution, a camera Sony DSC-HX5V with 10 megapixels and internal GPS sensor was also used.

The flight was followed through a remote controller wirelessly connected with an Apple iPad Air 2.

In the study area 1, a manually piloted flight-mode was carried out due to the lack of coverage of UMTS signal causing, in turn, the complete absence of internet connection. The manual flight paths were organized into three different acquisition methods: (a) three aerial strips at three different altitudes: 30, 60, and 120 m above ground level, shooting the photos perpendicular to the flight direction; (b) two aerial strips very close (3 and 5 m) to the fault plane, with the oblique-oriented camera at 45 degrees; (c) two aerial strips farther from the previous one, with photos shot perpendicular to the outcrop (Figure 2a,b). A total of 268 photos were acquired, with a minimum front and side overlapping of 80%. During half of the flight, the camera orientation was maintained perpendicular to the main path, whereas, for the second half-flight, a path-parallel arrangement was set. The need to adopt different shooting angles was due to the high slope-angle characterizing the outcrops of this sample area.

In the study area 2, the consistently good internet connection allowed to plan an automatic-mode guided flight through a dedicated application.

In this case, the flight path was planned to maintain a constant elevation of 70 m above ground level (Figure 2c,d). In the second study area, four aerial sweeps were carried out, leading to the acquisition of 100 photos, with overlapping (both in front and side) ranging from 60% to 65%. During the flight, as this area was completely flat, the camera orientation was maintained perpendicular to the main path, and the images were acquired automatically.

2.3.3. Photogrammetric Processing

Photogrammetric processing was performed using a Laptop HP Omen 17-an002nl with 3.8 a GHz (in Turbo Boost, 6 MB of cache, 4 core) Intel Core i7-7700HQ, 32 GB RAM (2×16 GB DDR4-2400), NVIDIA GeForce GTX 1070A (8 GB GDDR5) and SSD 512 GB PCIe NVMe M.2, running Agisoft Metashape Professional Software.

The processing with Agisoft Metashape software was necessary to obtain a spatial resolution of ~ 1 cm/pixels for virtual outcrops reconstruction. Digital photogrammetry, obtained from the sequential drone-acquired overlapping images and through the use of Agisoft Metashape software led to the following elaborations: (a) sparse point clouds, (b) dense point clouds, (c) meshes and textures, (d) 3D models, (e) tiled models, (f) DEM and orthomosaic model.

Figure 5 shows all the processing steps carried out with Agisoft Metashape software (details in the caption of Figure 5).

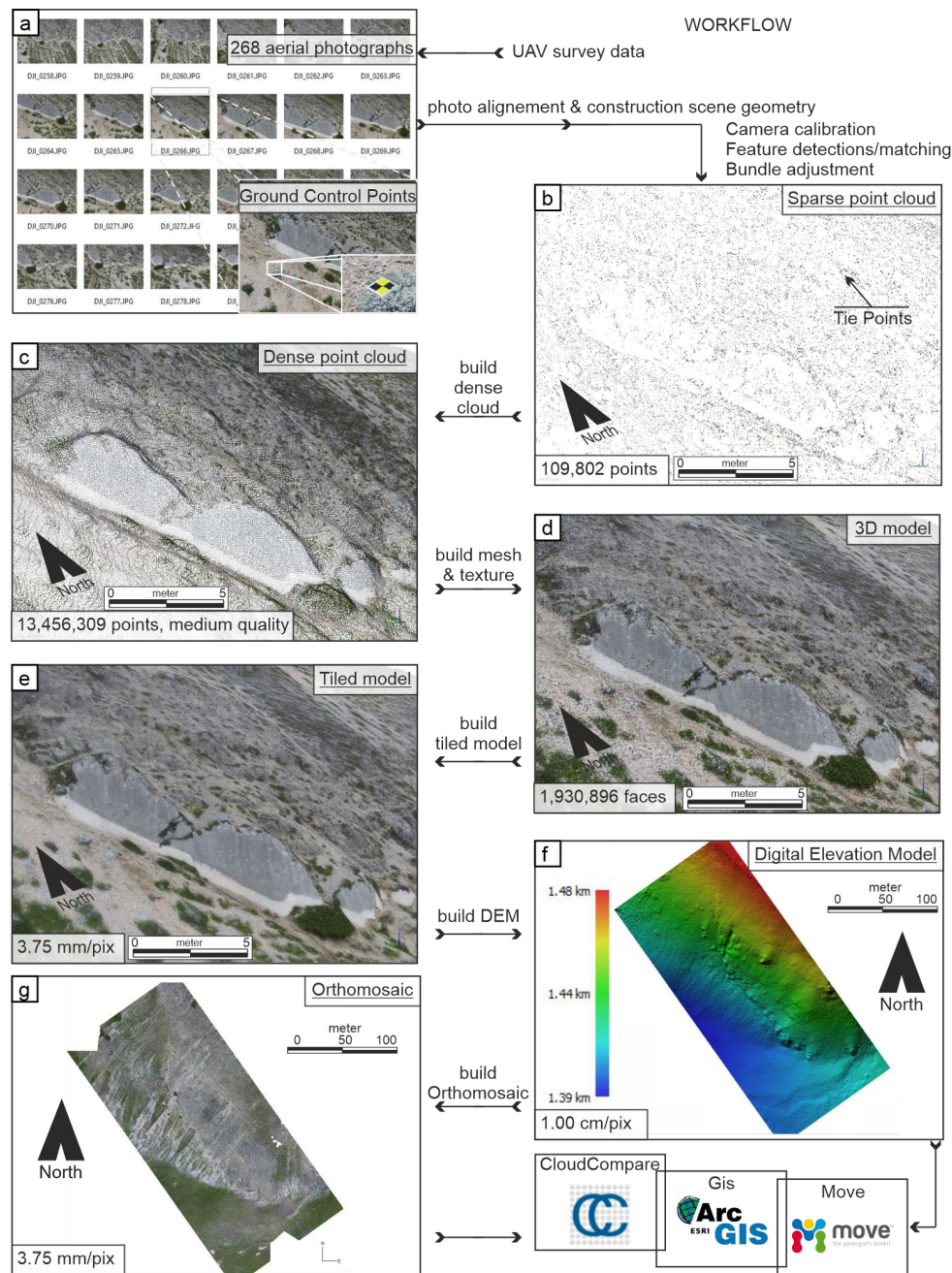


Figure 5. Workflow of the used digital photogrammetry procedure in the sample area 1 (a to g are in-sequence steps): (a) overlapping digital aerial photographs and ground control points are imported into the software package; features within the images are automatically detected, matched, and used to calculate locations and orientations of camera shooting points; (b) points that have been used for the image alignment form an initial sparse-point cloud (109,802 points); the inclusion of ground control points make the sparse-point cloud automatically georeferenced; (c) point densification (multi-view stereo algorithm): points that were manually classified as representing the ground surface are exported as a dense-point cloud (over 13 millions points); (d) 3D model construction obtained building meshes between dense-point cloud, with 1,930,896 faces; (e) a tiled model is obtained by interpolations of all image acquired during drone survey with faces of 3D model, the final resolution is 3.75 mm/pixel; (f) Construction of DSM containing all height values through rasterizing the dense-point cloud or from meshes. The obtained Digital Surface Model has a resolution of 1.00 cm/pixel; while (g) the georeferenced orthomosaic with a high resolution of 3.75 mm/pixel was reconstructed interpolating all the photos shot from the drone. Additional datasets were computed for fracture mapping in a Cloud Compare, ArcGIS, and Move Petex suite software.

2.3.4. Extraction of Fault Slip Data from Cloud Compare

The Cloud Compare [<http://www.danielgm.net/cc/>] open-source software allowed to perform structural geological analysis of the surveyed coseismic ruptures, directly on a desktop PC. The generated 3D point cloud, including more than 13 million points (Figures 5c and 6), georeferenced in the previous steps, were used to reconstruct the virtual outcrops and for the subsequent kinematic analysis on the fault planes.

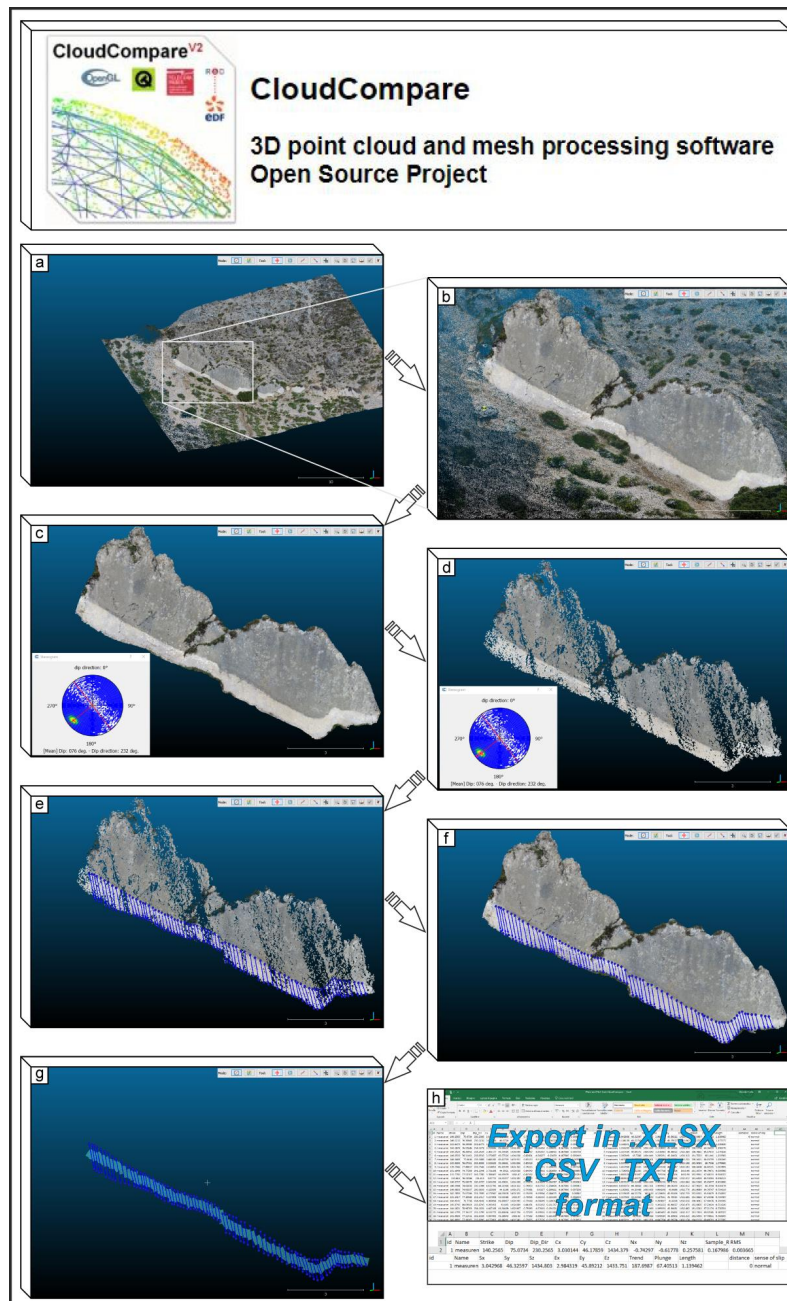


Figure 6. The main steps carried out in Cloud Compare (CC): (a) dense-points cloud imported into a CC as ascii file; (b) selection of the interest features; (c) contour and selection of all the dense-point cloud around the fault plane and extraction, through the plugin qFacets, of all plunge and dip direction in a stereogram; (d) from the stereogram the dip directions of the striae, evidenced by grooves, are excluded; (e,f) picking of net displacement (mm), striae attitude (trend and plunge), dip direction and dip-angle of the fault plane; (g) view of the net displacement and the striae detected on the fault plane; (h) export all data in excel, .csv, or .txt format.

After the processing of the CAB virtual outcrop, the surface of the ~15 m long fault mirror was manually extracted from the density point cloud.

Using the Cloud Compare software, and particularly the plugin qFacets [43] ([https://www.cloudcompare.org/doc/wiki/index.php?title=Facets_\(plugin\)](https://www.cloudcompare.org/doc/wiki/index.php?title=Facets_(plugin))), it was possible to make observable the long-term striae through an “interactive stereogram” (see inset in Figure 6c,d). In fact, by selecting a narrow range of values of dip direction and dip angle, the plugin makes visible only a few facets of fault plane (i.e., as the ridges in grooves lineations). This application of interactive filtering is exceedingly useful to understand the trend of the lineations on the outcrop in a tridimensional space. After choosing and comparing them with the 30 October coseismic slip vector, measured directly in the field (correlating hanging wall and footwall piercing points), the associated net displacement was assessed. Through a “virtual compass” on Cloud Compare, the outcrop orientation was determined, and the use of the “lineation tool” allowed the measurement of the height and dip directions of the coseismic slickenlines. Finally, through Cloud Compare software, all the extracted data obtained from the measurements on the virtual outcrop, were exported in .csv format file, as dip, dip-azimuth, trend and plunge, and plotted onto stereonet for structural analysis.

The described steps are shown in Figure 6, from dense-point cloud import (a) to the extraction of the fault plane (b), to the measurement of coseismic elements (total or net displacement, c–g) until exporting of the database (h) in excel, csv, or txt format.

2.3.5. High-Resolution Topographic Profiling

To optimize the quality of the result of our topographic analysis, we used two different software to extrapolate profiles from the Digital Surface Model, which led to obtaining 1 cm resolution over area 1 and a resolution of 3 cm in area 2 (Figure 7a–d). In particular, serial profiling across the coseismic ruptures of both CAB and PTP fault was performed through the Esri ArcGis v.10.x “3DAnalyst” and through the “Create Sections” tool of Move 2019. From both the sets of profiles, we estimated the fault-scarp height (Figure 7a–d).

To compare our digital field data with those obtained by aero-photogrammetric 3D model, several fault attitudes along the CAB were manually collected, and the height of the scarps measured (Figure 7b).

The “surface control” is essential to estimate the errors between analogical (real outcrop) and digital (virtual outcrop) measurement data.

In the field, a meter stick was used to estimate all along the fault trace, the height of the scarp, associated throw, and net displacement, both on the long term and coseismic free face. The slope dip angle was measured using a clinometer (Figure 7b).

Then, we compared the morphological height, the strike, the dip, and dip azimuth of the fault plane, measured in the field, with those obtained from the virtual outcrop 3D model.

The observed deviation between the height values of the fault scarp directly measured in the field and those extracted from virtual outcrop never exceed 2 cm (compare the deviations between the curves and the colored dots of Figure 8b), confirming the reliability of the reconstructed digital topography.

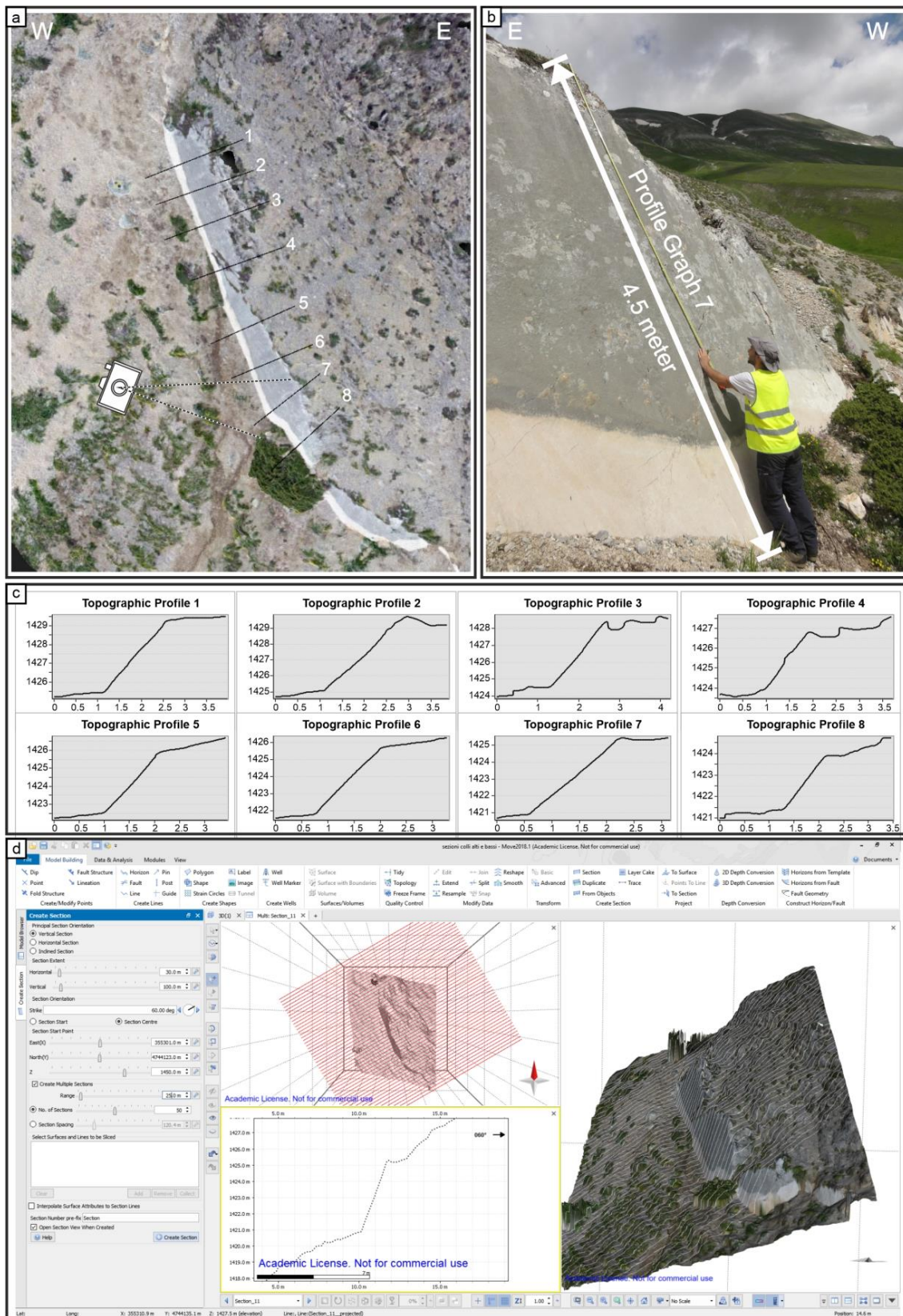


Figure 7. Georeferenced orthomosaic of CAB. (a) Digital Surface Model (DSM) of CAB and trace of topographic profile (from 1 to 8); (b) manual measuring of the scarp height associated to the CAB; (c) topographic profiles obtained using 3D Analyst extension of ESRI ArcGis; (d) topographic profiles obtained through move software.

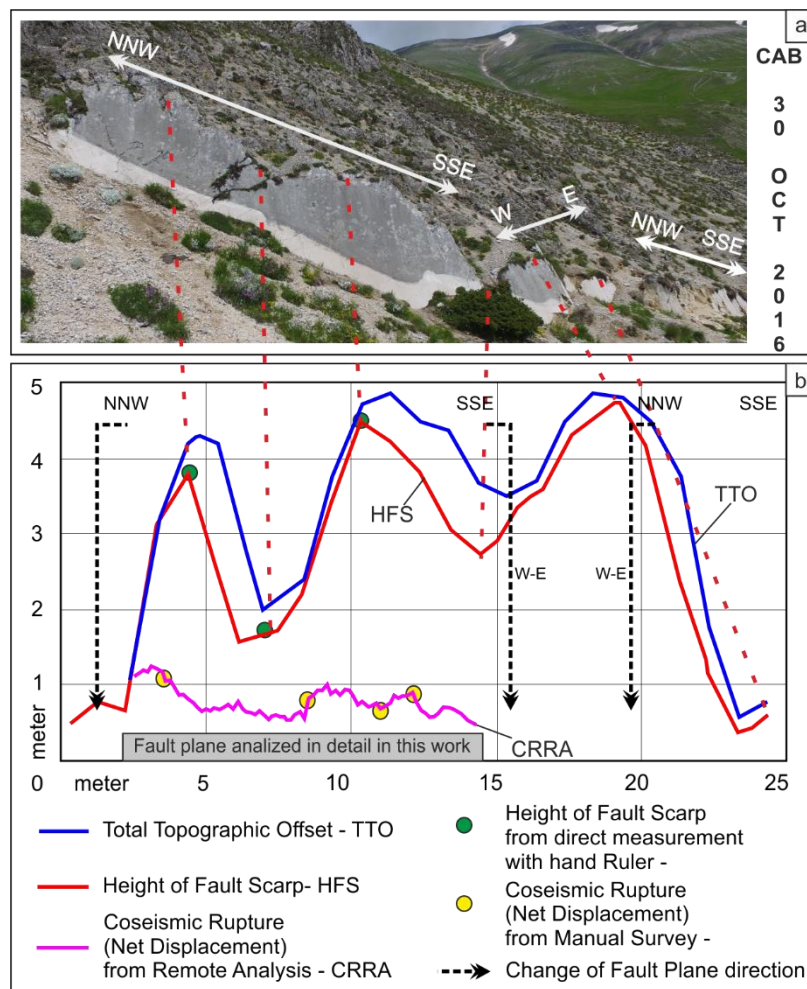


Figure 8. (a) Outcrop image of the CAB fault; (b) Comparison of different types of topographic profiles; blue line: height of long term slope; red line: effective present fault scarp; violet: coseismic net displacement. Both along-strike distance (abscissa) and height values (ordinate) are expressed in meters. Colored dots refer to field measurements collected at control points.

3. Results

3.1. Study Area 1—Colli Alti e Bassi Fault (CAB)

3.1.1. Topographic Analysis of CAB

The graphs in Figure 8 show a comparison between the measures of the Total Topographic Offset (TTO = blue line), the Height of the preserved Fault Scarp (HFS = red line) and the 30 October 2016 Coseismic Ruptures (net displacement) from Remote Analysis (CRRA= violet line) measured on the CAB in the sample area 1.

The estimated values of these features (on the Y axis, in meters) are plotted against the along-strike distance of each measurement point (abscissa) from the northern tip point of the fault-scarp outcrop (assumed as X = 0).

Dots in the Figure 8 graph mark the values, manually measured on the control points, respectively, for the height of the fault scarp, measured with hand ruler (green dots), and the 30 October 2016 coseismic ruptures (net displacement) from the manual survey (yellow dots). The good agreement between the field data and the assessments obtained from the topographic analysis on the virtual outcrop, confirms the reliability of the adopted method.

The TTO and HFS curves show very similar trends but differ in several points because the former includes the part of the scarp removed by erosion.

Interestingly, the CRR curve, even if characterized by lower values (higher observed net slip = 1.25 m), shows a good correlation with TTO and HFS curves, as regards the position of the maxima and minima. This remarkable consistence suggests that the along-strike height profile of the current fault scarp derives from the add up of a certain number of coseismic displacements, each characterized by slip-profiles similar to the one caused by the mainshock of the 2016 sequence.

3.1.2. Structural and Kinematics Analysis of the CAB

During the fieldwork, several attitudes of the CAB were measured as a dip and dip azimuth, using either a traditional compass-clinometer and a Fieldmove-equipped Apple iPad. After data collection, the whole dataset was managed in a georeferenced digital database.

Subsequently, we extracted attitude and kinematic data from the virtual outcrop reconstructed through remotely acquired images (see Section 2.3.4)

A comparison between the three different attitude datasets is shown in Figure 9.

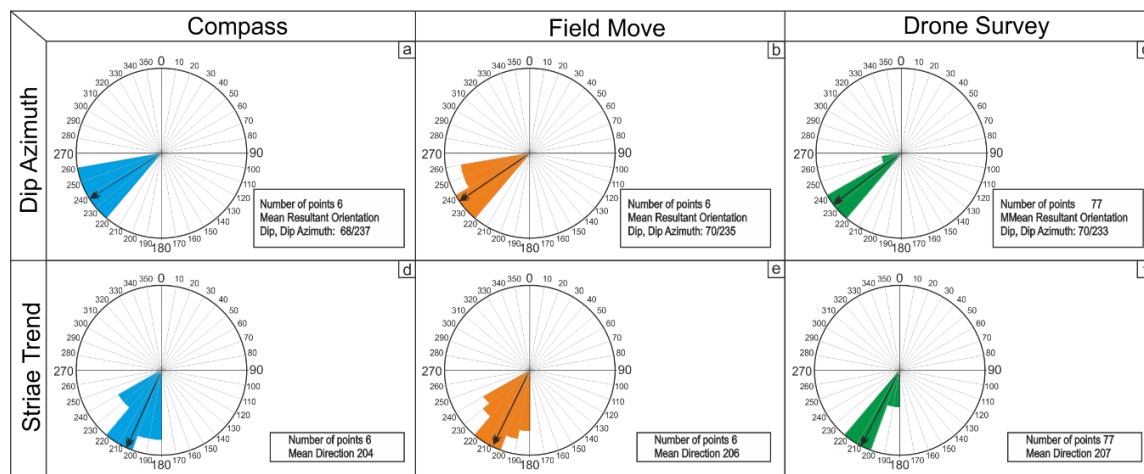


Figure 9. Comparison between the fault attitude and striations trends measured through high-resolution sampling on the CAB using traditional compass-clinometer (a,d), Fieldmove App on a digital device (b,e), and virtual outcrop reconstructed from drone-acquired imagery (c,f). The upper plots (a–c) shows the fault dip-azimuth; the lower plots (d–f) shows the trend of associated striae; for each rose diagram, the mean value resulting from the statistical analysis of the dataset is reported in the bottom-right rectangle. Rose diagrams were extracted through Move 2019 software and redrawn through Corel Draw X4 software.

The hand-compass collected dataset shows that on six measurements on the fault plane, the trend of dip-azimuth is variable between N220 and N260, with a mean resultant plane orientation of dip-azimuth at N237 and dip-angle of 68 degrees (Figure 9a). In the same points, the measurements with the Fieldmove app show a dip-azimuth trend on a fault plane, comprised between N220 and N260, with a mean resultant plane orientation of dip-azimuth at N235 and dip-angle of 70 degrees (Figure 9b). However, the results obtained from virtual outcrop, clearly with a huge number of data (77 points measurements), shows a main dip-azimuth trend between N220 and N240 and only a few data comprised between N240 and N260; also in this last case, mean dip-azimuth of the fault plane orientation shows a trend of N233 and dip-angle of 70 degrees (Figure 9c).

In order to compare the measures of the striation trend collected through three different used tools (Figure 9d–f and Table 1), a number of six data were also acquired using hand-compass and Fieldmove integrated compass. In both cases, the dispersion of data varies in the range between N180 and N240, except for the huge data extracted from the virtual outcrop that shows an attitude between N180 and

N220 and the mean direction dipping toward N207, well comparable with data acquired with the previously described tools.

Table 1. Summary table of the data collected with the different instruments (Compass, Fieldmove, Aero-Photogrammetric survey).

Colli Alti e Bassi Fault—CAB					
FAULT ATTITUDE					
INSTRUMENTS	DIP AZIMUTH Min-Max value	DIP ANGLE	STRIAE TREND Min-Max value	MEAN RESULTANT PLANE ORIENTATION	STRIAE TREND
Hand Compass	N220-N260	66–72	N180-N240	N237/68°	N204
Fieldmove App	N220-N260	67–73	N180-N240	N235/70°	N206
Drone Survey	N220-N240	66–74	N180-N220	N233/70°	N207

As regards the determination of fault attitude data, the good degree of mutual correlability between the differently acquired data is evident and encouraging. In fact, they mostly agree in providing an average fault attitude of~ a 235/70 (dip-notation value, compare rose diagrams Figure 9a–c,d–f and Table 1). From such a point of view, the remote sensing survey is advantageous, considering the large number of data collected over a very short time in comparison with both the traditional and digital field mapping techniques.

3.2. Study Area 2—Prate Pala Fault (PTP)

Topographic Analysis of PTP

Despite the small offset associated with the 30 October coseismic rupture, the reactivation of the PTP has highlighted soon after the mainshock thanks to the displacement of the paved road (S.P.477) from Forca di Presta to Castelluccio di Norcia (Figure 3g,h). A maximum offset of 14 cm was measured in the field in the central part of the coseismic rupture (Figure 3f), whose total length was estimated in ~1.3 km, our data are well comparable with the results obtained in Villani & Sapia 2017 [44].

The performed drone-aided mapping, which allowed the detection of tectonic scarps displacing the flat topography of the Castelluccio di Norcia plain, led to reconstruct a 3 cm resolution Digital Surface Model (DSM).

DSM models elaborated using this technique also allow removal of vegetation noise. Fortunately, in the studied cases, this problem was negligible because the periods in which the aerial images were acquired (beginning of November 2016 and afterward in 2018), were preceded by several months of intense grazing with poor grass regrowth, due to deficient rainfall.

Further processing of the DSM allowed to explore and analyze through the functions of the ArcGIS tools, the slope analysis, the shaded relief, and the aspect of the fault scarp.

A set of 27 topographic profiles, perpendicular to the fault scarp, were drawn to investigate the morpho-structural expression of the PTP (Figure 10) and to reconstruct the along-fault coseismic slip profiles, from north to south.

The systematical counter-slope (i.e., dipping towards east, thus opposite to the fault dip) topography observed west of the PTP trace is interesting, suggesting a back tilting of the hanging wall block, which is coherent with the normal kinematic of the fault.

This observation, confirmed by the persistence of a long-term topographic scarp resistant to the intense breeding and plowing practiced in the area, provides further evidence of the present activity of the PTP.

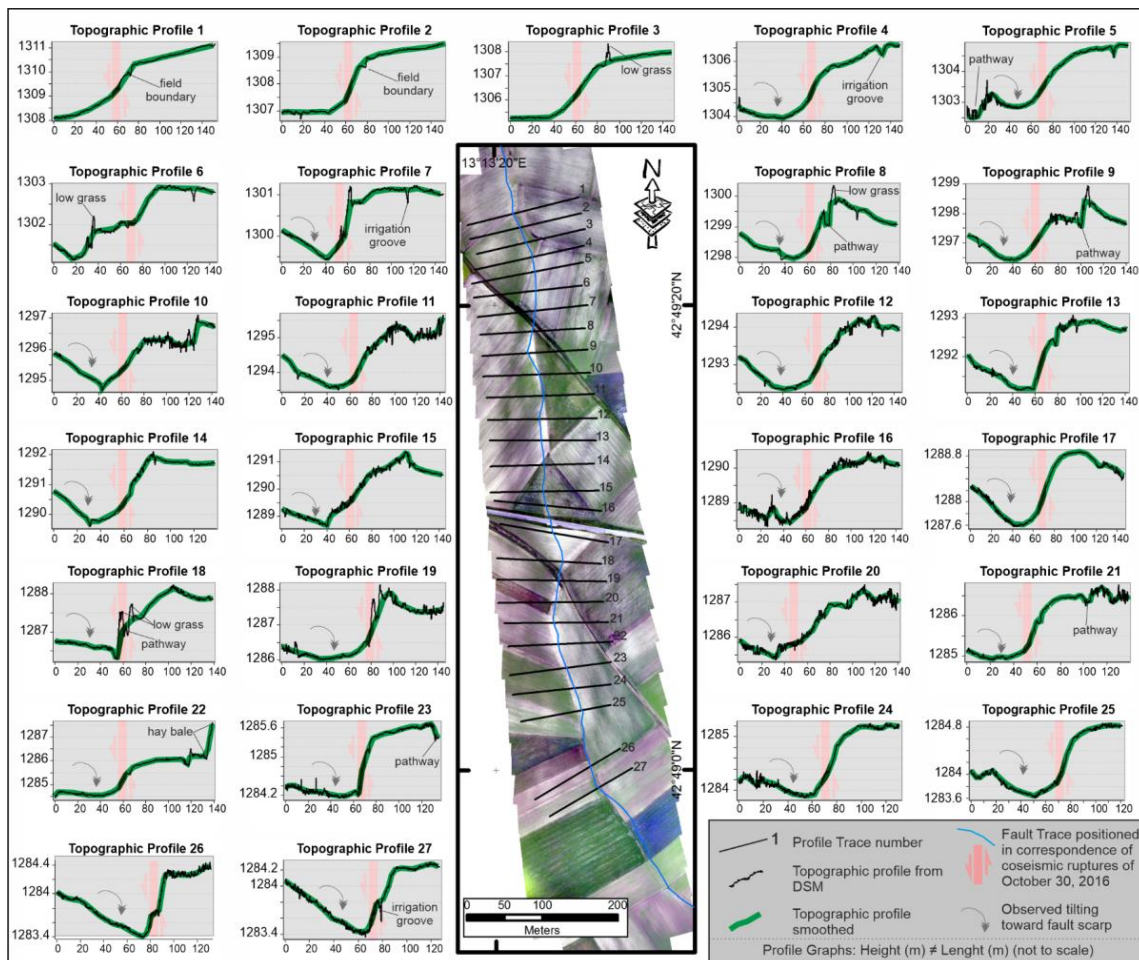


Figure 10. Topographic profiles generated using “3D analyst” in the ArcGis platform (Orthomosaic Photo and DSM have a resolution of 3 cm per pixel).

A comparison between the along-strike DSM-derived topographic offset and the coseismic slip profile is shown in Figure 11.

In the first case (Figure 11a), from the northern edge of PTP, the profile increases with a medium-high slope reaching the maximum height where the topographic scarp is ~2.3 m. Moving south, the scarp shows a gradual decrease to zero at the southernmost surface tip of the PTP. The observed asymmetric trend of the topographic offset suggests, according to Manighetti [45] and Cappa et al. [46], that, during previous events, surface ground rupture propagated mainly from north to south. On the contrary, in Figure 11b, the trend of the coseismic slips shows an opposite triangular shape compared to the previous one, culminating at a maximum value of 14 cm (Figure 3f).

The aforesaid works [45,46], investigating the distribution of the slip along with the fault segments during the coseismic rupture, interpreted the triangular shape, characterizing both the profiles as due to the dynamics of rupture propagation.

In particular, Manighetti et al. [45] show, from the analysis of several normalized displacement profiles, that the geometry of the coseismic slip profile gives information on the polarity of the rupture propagation and the location of the epicenter from the fault tips and the point of maximum displacement.

Brozzetti et al. [15], comparing the 2016 Central Italy coseismic ruptures with the surface faulting of the global earthquakes, agreed with the suggestion of Manighetti et al. [45], showing that the coseismic slip profiles obtained from the field survey have an asymmetric shape (from south to north) for the whole VBF, and also for the single VRS, VBS, and CUS segments of the master fault.

Similarly, the here reported data suggest a polarity of fracture propagation from south to north, as shown by the asymmetry of the graphs Figure 11b.

Possibly the difference in the observed polarity of propagation may depend on the hypocenter location and the magnitude of the earthquakes that provide surface faulting.

Moreover, according to Tao et al. [47] and Iezzi et al. [41,48], the aspect of the surface faulting is influenced by fault geometry and, in particular, fault segmentation and/or change of direction (bending). It is to be taken into account that this work had the opportunity to analyze only a short section of the PTP fault, whose effective length is reasonably much higher than the portion ruptured at the surface during the 30 October mainshock.

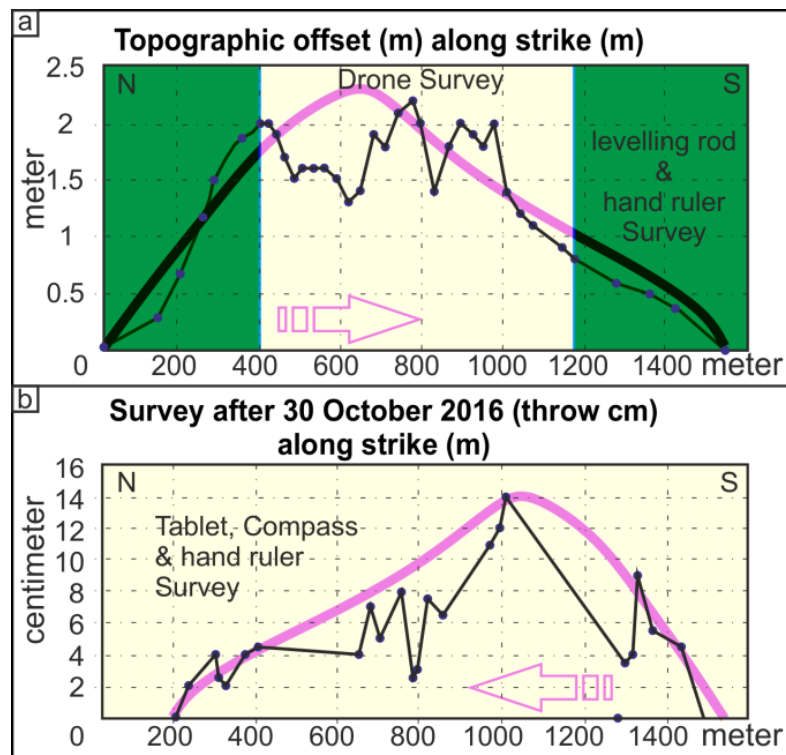


Figure 11. Comparison between the topographic fault scarp ((a), in meters) and the coseismic slip profile ((b), centimeters) surveyed following the 30 October 2016 earthquake (Mw 6.5) along the PTP.

In Figure 12b,c the measures of coseismic ruptures from hand compass and tablet device are showed whereas Figure 12d displays the direction of fault scarp attitude obtained from DSM analysis.

Comparing the three rose diagrams, we observe that the coseismic ruptures mostly strike in the same direction of the scarp generated from the ancient earthquakes even if, in a few cases, they show oblique directions. The fact that the coseismic ruptures are localized on the long-term fault scarp suggests a preferential growth of the central part of the fault during each seismic event.

The three rose diagrams of Figure 12b–d, reporting on the PTP attitudes measured with the different methods, show a substantial agreement (particularly the b,c ones) but also a certain dispersion. We interpret the latter as due to the remarkable differences in the number of acquired data. In fact, the major deviations occur when the hand compass and Fieldmove collected data are compared with data extracted from virtual outcrops. The 30 October coseismic ruptures were not measured from DSM because the aerophotogrammetric image resolution was insufficient to detect them. A lower elevation flight would have been necessary, especially in the areas of maximum slip, but unfortunately, when this high-precision mission was planned, the area had been erased by agricultural activities, hampering the acquisition of new images useful for making these measurements.

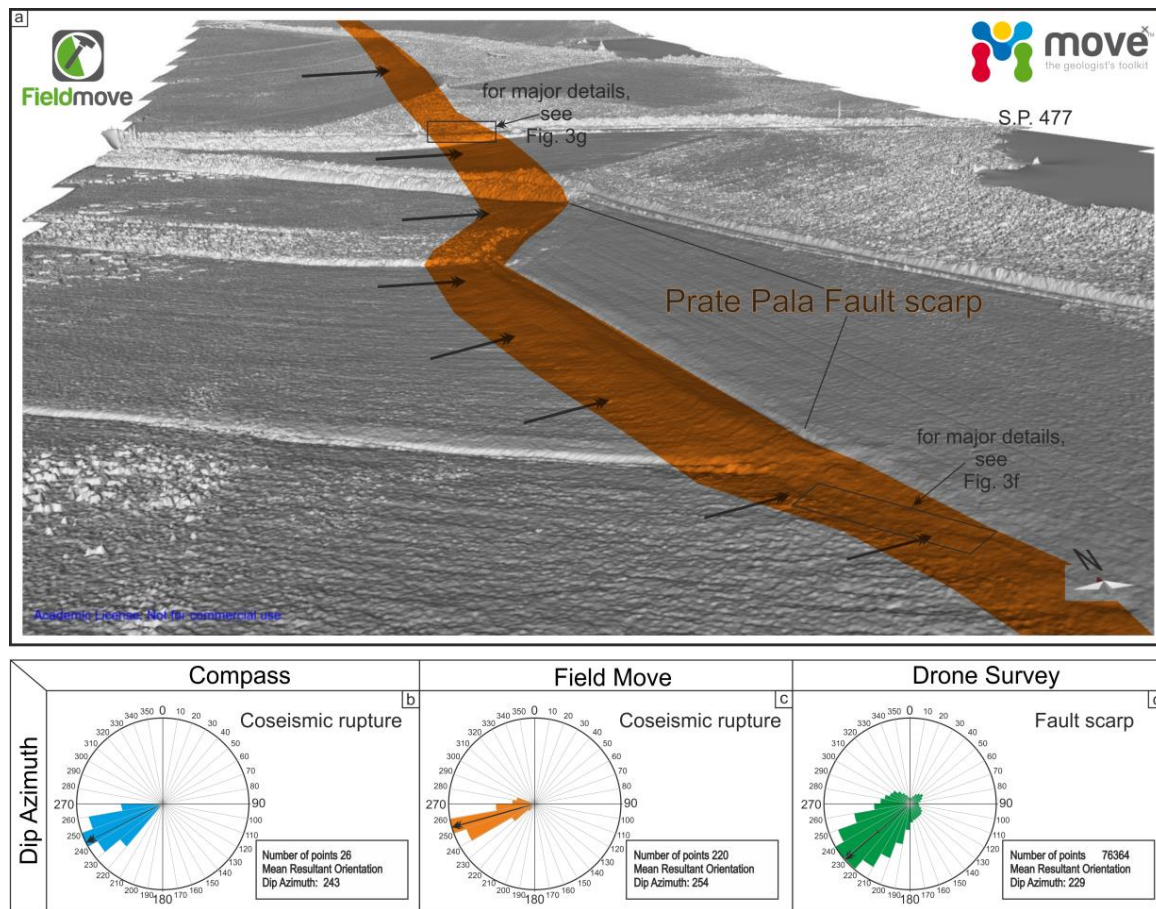


Figure 12. (a) Sample area 2: perspective 3D view extracted from Move Software of the PTP fault scarp in the Piano Grande near Castelluccio di Norcia; arrows show the alignment of the coseismic surface ruptures; in orange, the fault scarp of PTP is highlighted, black rectangles indicate the location of Figure 3f,g of coseismic ruptures measured during the field survey after 30 October 2016 Mw 6.5 earthquake (b,c) The plots show dip-azimuth of the coseismic ruptures measured with hand-compass and fieldmove; (d) trend of fault scarp obtained from a drone survey; for each rose diagram, the mean value resulting from the statistical analysis of the dataset is reported in the bottom-right rectangle Rose diagrams were extracted through Move 2019 software and redrawn through Corel Draw X4 software.

3.3. Accuracy and Precision

The integration of images acquired from a GPS/GNSS Drone has allowed placing of the virtual outcrop in its geographical position, with some limitations in terms of absolute accuracy. For most of the structural geology analysis, which did not need very-high accuracy in terms of geographical positioning, the described method can be considered satisfactory.

It is emphasized that this approach has to be considered as an integration to the “traditional” structural geological analysis. From the previous sections, it is evident that, in the two sample areas, the results obtained from aerophotogrammetrical processing and direct field measurements are comparable and that their precision is good. The maximum error measured along the fault scarps was close to 1 cm in the first area (CAB), and around 1–3 cm in the PTP area.

It is also to be considered that many sites, which may be potentially be studied using the proposed approach, are unreachable with bulky and heavy instrumentation.

In our case studies, the low performance of the GPS installed on the drone allowed correct positioning in a geographical system, but without a centimetric or millimetric accuracy. In any case, the precision of the height, width, and length of the virtual outcrop was satisfactory, thanks to the

correct use of caliber instruments. In conclusion, the results here obtained made it possible to create a valid and reliable model.

4. Discussion

The application of our working method to two study areas affected by coseismic surface faulting in 2016 Central Italy seismic sequence demonstrates that the virtual outcrop models represent an important tool for structural-geological and geomorphological research aimed at identifying and characterizing active tectonic structures.

Furthermore, comparing the information obtained from the morphological analysis of the fault scarp of CAB, with configuration of the coseismic surface faulting of the 2016 Central Italy seismic sequence, it is possible to make inferences on the rupturing history of the studied faults.

The good fit between the profile of the height of fault scarp and the 2016 coseismic slip profile (Figure 8b) suggests that the long-term fault scarp may have been formed as a result of several earthquakes, each causing a similar amount of surface displacement. It is also possible to infer for these events comparable values of magnitude.

In particular, taking into account: (i) the height of the entire fault scarp (ii) the amount of the 30 October 2016 coseismic slip, (iii) the geometry of the slope profiles also including the possible eroded free face, and (iv) the assumption that earthquakes of equal/similar magnitude generated equal/similar dislocations (compared to 2016 one), we hypothesize that at least five events are needed to reach the observed values of fault scarp height.

Previous paleoseismological works [16,49,50] have highlighted several seismic events, some of which caused the PTP reactivation, which occurred in the Pano Grande-Mt Vettore area. In particular, four events have been recognized in the last 8000 years, in addition to the earthquake of 2016. These four earthquakes, would have been occurred (from the oldest): (i) between IV and VI millennium BC, (ii) at the end of IV millennium BC, (iii) between II and III millennium BC, (iv) between the end of III and IV century AC (maybe in 270 AC). Furthermore, accepting the inferences, which implies that the 4.5 m outcropping fault scarp of the CAB was exhumed after the Last Glacial Maximum L.G.M. (~18.000 ky), a preliminary estimate of the slip rates, of 0.25 mm/y is obtained.

Of course, the analyzed fault scarps might have recorded a higher number of coseismic slip events, which could have been followed by erosional episodes in a longer geological time; thus, the above estimate must be considered purely indicative.

Several authors studied the causes/effects of the 2016 earthquakes from many points of view, as structural-geology, geophysics, seismology, paleoseismology, geomorphology, interferometry, geodesy, hydrogeology, engineering [15,31,32,34–36,39,40,51–91], but only a few authors have provided and elaborated data acquired through drones [92–95]. In addition, there are no author-produced image analyses of coseismic ruptures employing the techniques we propose here. Our results, obtained from the elaboration of high-resolution topography, fit well with the data published in Villani et al. [36], Brozzetti et al. [15], and Perouse et al. [95], acquired through traditional or digital mapping techniques. At the same time, the present work has improved the details of the surveyed geological features, some of which were not appreciable directly in the field; among this latter, the degradation and erosion of the fault plane as well as the tilting of the topographic surface, the dip-angle, and the off-fault width of the tilted area.

The here obtained results showed that the use of the drone-derived photogrammetry presents acceptable errors for all those structural-geological applications, also those that need high precision (near centimetric resolution), and that might be an integration to the traditional field survey.

In Figure 13, three types of DEMs with different resolutions (10 m, 5 m, and 1 cm) are compared.

The significant image resolution improvement of the topographic model obtained in this work (Figure 13c) is evident, as well as significant improvement of the geological interpretation, for example, in the correct positioning of tectonic structures.

High-resolution topography allows us to delineate with high precision the fault trace and in some conditions, such as in the CAB case, to identify the long term and recent kinematic indicators.

In cases where active faults displace post-LGM slopes, the applied procedure improves the estimates of the scarp height, thus helping to make inferences on the associated slip rates.

Moreover, improving the precision of the fault mapping (e.g., in Figure 13c) can, in turn, facilitate the identification of sites aimed at paleoseismological trenching.

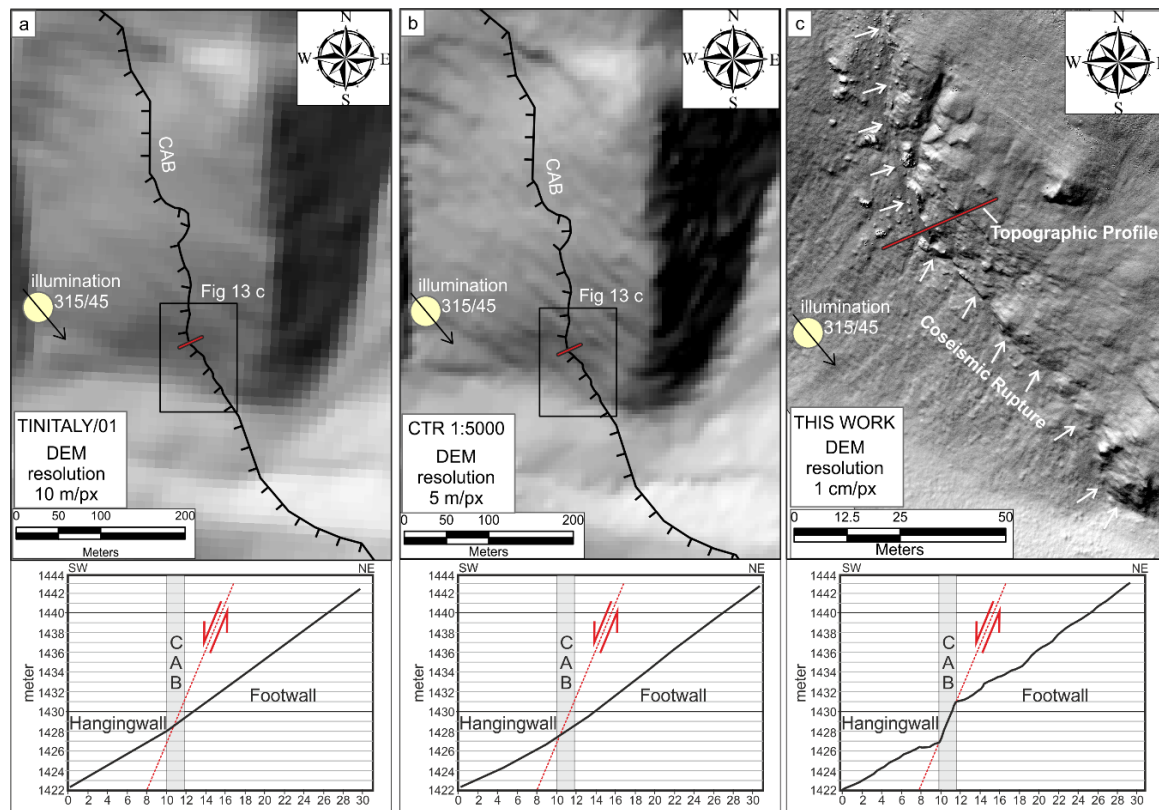


Figure 13. Comparison of DEM and detailed topographic profile obtained from: (a) TINITALY/01 <http://tinality.pi.ingv.it/> [96] with a resolution of 10 m per pixel; (b) Cartografia Tecnica Regionale 1:5000 scale from Regione Umbria [<http://www.umbriageo.regione.umbria.it/pagina/distribuzione-carta-tecnica-regionale-vettoriale-1-000>], with a resolution of 5 m per pixel; (c) 1 cm per pixel obtained from this work.

5. Conclusions

During routine geological fieldwork, faults are generally surveyed on topographic and geological maps using a traditional compass-clinometer or, when a high-resolution survey is needed, using a digital device (smartphone or tablet) with a dedicated application.

In this paper, we have shown that the use of Fieldmove app for digital devices integrated with the use of drone-acquired imagery is a performing combination, which speedily provides large sets of good-quality data, sensibly improving the topographic and geological models that are subsequently reconstructed.

The presented high-resolution aerial survey represents the first attempt to digitally reconstruct recent coseismic fault ruptures in variable geomorphological and outcrop conditions and to compare them with large published datasets collected through traditional and digital mapping.

In the study cases, which refer to two active splays of the Vettore-Bove Fault affected by surface faulting during the 2016 Central Italy seismic sequence, we reconstructed the fault traces, the height of the fault scarps, the amount of associated coseismic slip and its along-strike variations, with a precision that is much higher compared to previous literature reconstructions [15,29,36,37,97].

For all the aforesaid parameters, the estimated errors range within a few centimeters, a value that is well below the standards required by routine structural geological survey and is also acceptable for precision estimates of coseismic ground deformations.

A complete workflow in which the entire procedure is described in detail is reported. It is divided into successive steps specifying all the necessary software and tools to be applied to obtain the topographic model of a study area.

Moreover, an assessment of the precision and applicability of point clouds derived by drone imagery is provided and also compared with the performances of the digital and analogic compass-clinometer.

Some further possible applications of the reconstructed models on the investigated active fault, f.i. slip rate estimate or reconstruction of the rupture history is described, suggesting possible correlations and integrations with the available paleoseismological data.

The results of this work highlight that photogrammetry can cover and improve the map resolution, where necessary, with low-costs compared to more expensive techniques like the LiDAR data acquisition, which are very costly and logistically complex to apply in many locations.

In other words, these methodologies can undoubtedly be a significant step forward in geological mapping as well as in structural and geomorphological research. They represent a field of work capable of remarkable development and perspectives in the near future.

Funding: This research received no external funding.

Acknowledgments: This work presents the main results of a research carried out by the author in the framework of CRUST (Inter-University Center for Tridimensional Seismotectonic Analysis <https://www.crust.unich.it/>) activities, following the 2016 Central Italy Seismic Sequence. It was supported by DiSPUTer Departmental (60%) and Brozzetti research (30%) funds by the renewal of a research grant to Daniele Cirillo. The author is grateful to Petex, who provided them with the Move, 2019.1 suite software licence; and their supervisor F. Brozzetti for the useful discussions, suggestions, and critical review of the manuscript.

Conflicts of Interest: The author declares no conflict of interest.

References

1. Buckley, S.J.; Ringdal, K.; Naumann, N.; Dolva, B.; Kurz, T.H.; Howell, J.A.; Dewez, T.J.B. LIME: Software for 3-D visualization, interpretation, and communication of virtual geoscience models. *Geosphere* **2019**, *15*, 222–235. [[CrossRef](#)]
2. Bonali, F.L.; Tibaldi, A.; Marchese, F.; Fallati, L.; Russo, E.; Corselli, C.; Savini, A. UAV-based surveying in volcano-tectonics: An example from the Iceland rift. *J. Struct. Geol.* **2019**, *121*, 46–64. [[CrossRef](#)]
3. Barlow, J.; Gilham, J.; Ibarra Cofrã, I. Kinematic analysis of sea cliff stability using UAV photogrammetry. *Int. J. Remote Sens.* **2017**, *38*, 16. [[CrossRef](#)]
4. Cawood, A.J.; Bond, C.E.; Howell, J.A.; Butler, R.W.H.; Totake, Y. LiDAR UAV or compass-clinometer? Accuracy; coverage and the effects on structural models. *J. Struct. Geol.* **2017**, *98*, 67–82. [[CrossRef](#)]
5. Corradetti, A.; McCaffrey, K.; De Paola, N.; Tavani, S. Evaluating roughness scaling properties of natural active fault surfaces by mean of multi-view photogrammetry. *Tectonophysics* **2017**, *717*, 599–606. [[CrossRef](#)]
6. Tavani, S.; Corradetti, A.; Billi, A. High precision analysis of an embryonic extensional fault-related fold using 3D orthorectified virtual outcrops: The viewpoint importance in structural geology. *J. Struct. Geol.* **2016**, *86*, 200–210. [[CrossRef](#)]
7. Vollgger, S.A.; Cruden, A.R. Mapping folds and fractures in basement and cover rocks using UAV photogrammetry, Cape Liptrap and Cape Paterson, Victoria, Australia. *J. Struct. Geol.* **2016**, *86*, 168–187. [[CrossRef](#)]
8. Bistacchi, A.; Balsamo, F.; Storti, F.; Mozafari, M.; Swennen, R.; Solum, J.; Tueckmantel, C.; Taberner, C. Photogrammetric digital outcrop reconstruction, visualization with textured surfaces, and three-dimensional structural analysis and modeling: Innovative methodologies applied to fault-related dolomitization (Vajont Limestone, Southern Alps, Italy). *Geosphere* **2015**, *11*, 2031–2048. [[CrossRef](#)]
9. Bemis, S.P.; Micklethwaite, S.; Turner, D.; James, M.R.; Akciz, S.; Thiele, S.T.; Bangash, H.A. Ground-based and UAV-Based photogrammetry: A multi-scale, high-resolution mapping tool for structural geology and paleoseismology. *J. Struct. Geol.* **2014**, *69*, 163–178. [[CrossRef](#)]

10. James, M.R.; Robson, S. Mitigating systematic error in topographic models derived from UAV and ground-based image networks. *Earth Surf. Process. Landf.* **2014**, *39*, 1413–1420. [[CrossRef](#)]
11. Johnson, K.; Nissen, E.; Saripalli, S.; Arrowsmith, J.R.; McGarey, P.; Scharer, K.; Williams, P.; Blisniuk, K. Rapid mapping of ultrafine fault zone topography with structure from motion. *Geosphere* **2014**, *10*, 969–986. [[CrossRef](#)]
12. James, M.R.; Robson, S. Straightforward reconstruction of 3d surfaces and topography with a camera: Accuracy and geoscience application. *J. Geophys. Res. Earth Surf.* **2012**, *117*, 17. [[CrossRef](#)]
13. Westoby, M.J.; Brasington, J.; Glasser, N.F.; Hambrey, M.J.; Reynolds, J.M. ‘Structure-from-motion’ photogrammetry: A low-cost, effective tool for geoscience applications. *Geomorphology* **2012**, *179*, 300–314. [[CrossRef](#)]
14. McCaffrey, K.J.W.; Jones, R.R.; Holdsworth, R.E.; Wilson, R.W.; Clegg, P.; Imber, J.; Holliman, N.; Trinks, I. Unlocking the spatial dimension: Digital technologies and the future of geoscience fieldwork. *J. Geol. Soc. Lond.* **2005**, *162*, 927–938. [[CrossRef](#)]
15. Brozzetti, F.; Boncio, P.; Cirillo, D.; Ferrarini, F.; de Nardis, R.; Testa, A. High-resolution field mapping and analysis of the August–October 2016 coseismic surface faulting (central Italy earthquakes): Slip distribution, parameterization, and comparison with global earthquakes. *Tectonics* **2019**, *38*, 417–439. [[CrossRef](#)]
16. Galadini, F.; Galli, P. Paleoseismology of silent faults in the Central Apennines (Italy): The Mt. Vettore and Laga Mts. Faults. *Ann. Geophys.* **2003**, *46*, 815–836. [[CrossRef](#)]
17. Koopman, A. Detachment tectonics in the central Apennines, Italy. *Geol. Eltraiectina* **1983**, *30*, 1–155.
18. Lavecchia, G. Il sovrascorrimento dei Monti Sibillini: Analisi cinematica e strutturale. *Boll. Soc. Geol. Ital.* **1985**, *104*, 161–194.
19. Bally, A.W.; Burbi, L.; Cooper, C.; Ghelardoni, R. Balanced cross-sections and seismic reflection profiles across the central Apennines. *Mem. Della Soc. Geol. Ital.* **1986**, *35*, 257–310.
20. Barchi, M. Integration of a seismic profile with surface and subsurface geology in a cross-section through the Umbria-Marche Apennines. *Boll. Soc. Geol. Ital.* **1991**, *110*, 469–479.
21. Calamita, F.; Pizzi, A.; Roscioni, M. I “fasci” di faglie recenti ed attive di M. Vettore-M. Bove e di M. Castello-M. Cardosa (Appennino umbro-marchigiano). *Studi Geol. Camerti* **1992**, 81–95. [[CrossRef](#)]
22. Coltorti, M.; Consoli, M.; Dramis, F.; Gentili, B.; Pambianchi, G. Evoluzione geomorfologica delle piane alluvionali delle Marche centro-meridionali. *Geogr. Fis. Dinam. Quat.* **1991**, *14*, 87–100.
23. Blumetti, A.M.; Dramis, F.; Michetti, A.M. Fault-generated mountain fronts in the central Apennines (Central Italy): Geomorphological features and seismotectonic implications. *Earth Surf. Process. Landf.* **1993**, *18*, 203–223. [[CrossRef](#)]
24. Pizzi, A.; Calamita, F.; Coltorti, M.; Pieruccini, P. Quaternary normal faults, intramontane basins and seismicity in the Umbria-Marche-Abruzzi Apennine Ridge (Italy): Contribution of neotectonic analysis to seismic hazard assessment. *Boll. Soc. Geol. Ital.* **2002**, *1*, 923–929.
25. Brozzetti, F.; Lavecchia, G. Seismicity and related extensional stress field: The case of the Norcia seismic zone. *Ann. Tecton.* **1994**, *8*, 38–57.
26. Calamita, F.; Pizzi, A. Recent and active extensional tectonics in the southern Umbro-Marchean Apennines (Central Italy). *Mem. Soc. Geol. Ital.* **1994**, *48*, 541–548.
27. Cavinato, G.P.; De Celles, P.G. Extensional basins in the tectonically bimodal central Apennines fold-thrust belt, Italy: Response to corner flow above a subducting slab in retrograde motion. *Geology* **1999**, *27*, 955–958. [[CrossRef](#)]
28. Galadini, F.; Galli, P. Active tectonics in the central Apennines (Italy); input data for seismic hazard assessment. *Nat. Hazards* **2000**, *22*, 225–270. [[CrossRef](#)]
29. Pierantoni, P.; Deiana, G.; Galdenzi, S. Stratigraphic and structural features of the Sibillini Mountains (Umbria-Marche Apennines, Italy). *Ital. J. Geosci.* **2013**, *132*, 497–520. [[CrossRef](#)]
30. Biella, G.; Lavecchia, G.; Lozei, A.; Piali, G.; Scarascia, S. In Primi risultati di un’indagine geofisica e interpretazione geologica del piano di S. In *Scolastica e del Piano Grande (Norcia, pg)*, I Convegno Annuale G.N.G.T.S.; Atti 1° Convegno Gruppo Naz. Geof. Terra Solida Roma; 1981; pp. 293–308. Available online: <https://ricerca.unich.it/handle/11564/505514?mode=full.23#.XyDyzecRVPZ> (accessed on 20 July 2020).

31. Villani, F.; Sapia, V.; Baccheschi, P.; Civico, R.; Di Giulio, G.; Vassallo, M.; Marchetti, M.; Pantosti, D. Geometry and structure of a fault-bounded extensional basin by integrating geophysical surveys and seismic anisotropy across the 30 October 2016 Mw 6.5 earthquake fault (central Italy): The pian grande di Castelluccio basin. *Tectonics* **2019**, *38*, 26–48. [[CrossRef](#)]
32. Chiaraluce, L.; Di Stefano, R.; Tinti, E.; Scognamiglio, L.; Michele, M.; Casarotti, E.; Cattaneo, M.; De Gori, P.; Chiarabba, C.; Monachesi, G.; et al. The 2016 Central Italy Seismic Sequence: A First Look at the Mainshocks, Aftershocks, and Source Models. *Seismol. Res. Lett.* **2017**, *88*, 757–771. [[CrossRef](#)]
33. Michele, M.; Di Stefano, R.; Chiaraluce, L.; Cattaneo, M.; De Gori, P.; Monachesi, G.; Latorre, D.; Marzorati, S.; Valoroso, L.; Ladina, C.; et al. The Amatrice 2016 seismic sequence: A preliminary look at the mainshock and aftershocks distribution. *Ann. Geophys.* **2016**, *59*. [[CrossRef](#)]
34. Lavecchia, G.; Castaldo, R.; de Nardis, R.; De Novellis, V.; Ferrarini, F.; Pepe, S.; Brozzetti, F.; Solaro, G.; Cirillo, D.; Bonano, M.; et al. Ground deformation and source geometry of the August 24, 2016 Amatrice earthquake (Central Italy) investigated through analytical and numerical modeling of DInSAR measurements and structural-geological data. *Geophys. Res. Lett.* **2016**, *43*, 12389–12398. [[CrossRef](#)]
35. Pucci, S.; De Martini, P.M.; Civico, R.; Villani, F.; Nappi, R.; Ricci, T.; Azzaro, R.; Brunori, C.A.; Caciagli, M.; Cinti, F.R.; et al. Coseismic ruptures of the 24 August 2016, Mw 6.0 Amatrice earthquake (central Italy). *Geophys. Res. Lett.* **2017**, *44*, 2138–2147. [[CrossRef](#)]
36. Open EMERGEO Working Group; Villani, F.; Civico, R.; Pucci, S.; Pizzimenti, L.; Nappi, R.; De Martini, P.M.; Agosta, F.; Alessio, G.; Alfonsi, L.; et al. A database of the coseismic effects following the 30 October 2016 Norcia earthquake in Central Italy. *Sci. Data Nat.* **2018**, *5*, 180049. [[CrossRef](#)]
37. Open EMERGEO Working Group; Civico, R.; Pucci, S.; Villani, F.; Pizzimenti, L.; De Martini, P.M.; Nappi, R.; Agosta, F.; Alessio, G.; Alfonsi, L.; et al. Surface ruptures following the 30 October 2016 Mw 6.5 Norcia earthquake; central Italy. *J. Maps* **2018**, *14*, 151–160. [[CrossRef](#)]
38. Livio, F.; Michetti, A.M.; Vittori, E.; Gregory, L.; Wedmore, L.; Piccardi, L.; Tondi, E.; Roberts, G. Central Italy Earthquake Working Group Surface faulting during the August 24, 2016, central Italy earthquake (Mw 6.0): Preliminary results. *Ann. Geophys.* **2016**, *59*, 1–7. [[CrossRef](#)]
39. Pizzi, A.; Di Domenica, A.; Gallovič, F.; Luzi, L.; Puglia, R. Fault segmentation as constraint to the occurrence of the mainshocks of the 2016 central Italy seismic sequence. *Tectonics* **2017**, *36*, 2370–2387. [[CrossRef](#)]
40. Marzocchi, W.; Taroni, M.; Falcone, G. Earthquake forecasting during the complex Amatrice-Norcia seismic sequence. *Sci. Adv.* **2017**, *3*, e1701239. [[CrossRef](#)]
41. Iezzi, F.; Mildon, Z.; Walker, J.F.; Roberts, G.; Goodall, H.; Wilkinson, M.; Robertson, J. Coseismic throw variation across along-strike bends on active normal faults: Implications for displacement versus length scaling of earthquake ruptures. *J. Geophys. Res. Solid Earth* **2018**, *123*, 9817–9841. [[CrossRef](#)]
42. Fieldmove user guide Midland Valley-Petroleum Experts. Available online: https://www.petex.com/media/2578/fieldmove_user_guide.pdf (accessed on 20 July 2020).
43. Dewez, T.J.B.; Girardeau-Montaut, D.; Allanic, C.; Rohmer, J. Facets: A cloudcompare plugin to extract geological planes from unstructured 3d point clouds. *Int. Arch. Photogramm. Remote Sens. Spatial Inf. Sci.* **2016**, *XLI-B5*, 799–804. [[CrossRef](#)]
44. Villani, F.; Sapia, V. The shallow structure of a surface-rupturing fault in unconsolidated deposits from multi-scale electrical resistivity data: The 30 October 2016 Mw 6.5 central Italy earthquake case study. *Tectonophysics* **2017**, *717*, 628–644. [[CrossRef](#)]
45. Manighetti, I. Evidence for self-similar, triangular slip distributions on earthquakes: Implications for earthquake and fault mechanics. *J. Geophys. Res.* **2005**, *110*, 25. [[CrossRef](#)]
46. Cappa, F.; Perrin, C.; Manighetti, I.; Delor, E. Off-fault long-term damage: A condition to account for generic, triangular earthquake slip profiles. *Geochem. Geophys. Geosyst.* **2014**, *15*, 1476–1493. [[CrossRef](#)]
47. Tao, Z.; Alves, T.M. Impacts of data sampling on the interpretation of normal fault propagation and segment linkage. *Tectonophysics* **2019**, *762*, 79–96. [[CrossRef](#)]
48. Iezzi, F.; Roberts, G.; Walker, J.F.; Papanikolaou, I. Occurrence of partial and total coseismic ruptures of segmented normal fault systems: Insights from the central Apennines, Italy. *J. Struct. Geol.* **2019**, *126*, 83–99. [[CrossRef](#)]
49. Galli, P.; Castenetto, S.; Peronace, E. The macroseismic intensity distribution of the 30 October 2016 earthquake in central Italy (Mw 6.6): Seismotectonic implications. *Tectonics* **2017**, *36*, 2179–2191. [[CrossRef](#)]

50. Galli, P.; Galderisi, A.; Peronace, E.; Giaccio, B.; Hajdas, I.; Messina, P.; Polpetta, F. Quante volte figliola? Confessioni Sibilline di una giovane faglia. In Proceedings of the Riassunti Estesi della Comunicazione, 36° Convegno Nazionale Gruppo Nazionale di Geofisica della Terra Solida, Trieste, Italy, 14–16 November 2017; pp. 41–45, ISBN 978-88-940442-5-6.
51. Bignami, C.; Valerio, E.; Carminati, E.; Doglioni, C.; Tizzani, P.; Lanari, R. Volume unbalance on the 2016 Amatrice-Norcia (central Italy) seismic sequence and insights on normal fault earthquake mechanism. *Sci. Rep.* **2019**, *9*, 4250. [[CrossRef](#)]
52. Brozzetti, F.; Mondini, A.C.; Pauselli, C.; Mancinelli, P.; Cirillo, D.; Guzzetti, F.; Lavecchia, G. Mainshock Anticipated by Intra-Sequence Ground Deformations: Insights from Multiscale Field and SAR Interferometric Measurements. *Geosciences* **2020**, *10*, 186. [[CrossRef](#)]
53. Cheloni, D.; De Novellis, V.; Albano, M.; Antonioli, A.; Anzidei, M.; Atzori, S.; Avallone, A.; Bignami, C.; Bonano, M.; Calcaterra, S.; et al. Geodetic model of the 2016 central Italy earthquake sequence inferred from insar and gps data. *Geophys. Res. Lett.* **2017**, *44*, 6778–6787. [[CrossRef](#)]
54. De Guidi, G.; Vecchio, A.; Brighenti, F.; Caputo, R.; Carnemolla, F.; Di Pietro, A.; Lupo, M.; Maggini, M.; Marchese, S.; Messina, D.; et al. Brief communication co-seismic displacement on October 26 and 30, 2016 (Mw 5.9 and 6.5)-earthquakes in central Italy from the analysis of a local GNSS network. *Nat. Hazards Earth Syst. Sci.* **2017**, *17*, 1885–1892. [[CrossRef](#)]
55. De Luca, G.; Di Carlo, G.; Tallini, M. A record of changes in the Gran Sasso groundwater before, during and after the 2016 Amatrice earthquake, central Italy. *Sci. Rep.* **2018**, *8*, 15982. [[CrossRef](#)] [[PubMed](#)]
56. Di Naccio, D.; Kastelic, V.; Carafa, M.M.C.; Esposito, C.; Milillo, P.; Di Lorenzo, C. Gravity versus tectonics: The case of 2016 Amatrice and Norcia (central Italy) earthquakes surface coseismic fractures. *J. Geophys. Res. Earth Surf.* **2019**, *124*, 994–1017. [[CrossRef](#)]
57. Durante, M.G.; Di Sarno, L.; Zimmaro, P.; Stewart, J.P. Damage to roadway infrastructure from 2016 central Italy earthquake sequence. *Earthq. Spectra* **2018**, *34*, 1721–1737. [[CrossRef](#)]
58. Ercoli, M.; Forte, E.; Porreca, M.; Carbonell, R.; Pauselli, C.; Minelli, G.; Barchi, M.R. Using Seismic Attributes in seismotectonic research: An application to the Norcia Mw = 6.5 earthquake (30th October 2016) in Central Italy. *Solid Earth* **2020**, *11*, 329–348. [[CrossRef](#)]
59. Ferrario, M.F.; Livio, F. Characterizing the distributed faulting during the 30 October 2016, central Italy earthquake: A reference for fault displacement hazard assessment. *Tectonics* **2018**, *37*, 1256–1273. [[CrossRef](#)]
60. Galadini, F.; Falcucci, E.; Gori, S.; Zimmaro, P.; Cheloni, D.; Stewart, J.P. Active faulting in source region of 2016–2017 central Italy event sequence. *Earthq. Spectra* **2018**, *34*, 1557–1583. [[CrossRef](#)]
61. Galderisi, A.; Galli, P. Offset component and fault-block motion during the 2016 central Italy earthquake (Mw 6.6, Monte Vettore fault system). *J. Struct. Geol.* **2020**, *134*, 11. [[CrossRef](#)]
62. Galli, P.; Galderisi, A.; Peronace, E.; Giaccio, B.; Hajdas, I.; Messina, P.; Pileggi, D.; Polpetta, F. The awakening of the dormant mount Vettore fault (2016 central Italy earthquake, Mw 6.6): Paleoseismic clues on its millennial silences. *Tectonics* **2019**, *38*, 687–705. [[CrossRef](#)]
63. Gentili, S.; Di Giovambattista, R.; Peresan, A. Seismic quiescence preceding the 2016 central Italy earthquakes. *Phys. Earth Planet. Inter.* **2017**, *272*, 27–33. [[CrossRef](#)]
64. Huang, M.-H.; Fielding, E.J.; Liang, C.; Milillo, P.; Bekaert, D.; Dreger, D.; Salzer, J. Coseismic deformation and triggered landslides of the 2016 Mw 6.2 Amatrice earthquake in Italy. *Geophys. Res. Lett.* **2017**, *44*, 1266–1274. [[CrossRef](#)]
65. Liu, C.; Zheng, Y.; Xie, Z.; Xiong, X. Rupture features of the 2016 Mw 6.2 Norcia earthquake and its possible relationship with strong seismic hazards. *Geophys. Res. Lett.* **2017**, *44*, 1320–1328. [[CrossRef](#)]
66. Masi, A.; Chiauzzi, L.; Santarsiero, G.; Manfredi, V.; Biondi, S.; Spacone, E.; Del Gaudio, C.; Ricci, P.; Manfredi, G.; Verderame, G.M. Seismic response of rc buildings during the Mw 6.0 August 24, 2016 central Italy earthquake: The Amatrice case study. *Bull. Earthq. Eng.* **2017**, *2019*, 5631–5654. [[CrossRef](#)]
67. Mazzoni, S.; Castori, G.; Galasso, C.; Calvi, P.; Dreyer, R.; Fischer, E.; Fulco, A.; Sorrentino, L.; Wilson, J.; Penna, A.; et al. 2016–2017 central Italy earthquake sequence: Seismic retrofit policy and effectiveness. *Earthq. Spectra* **2018**, *34*, 1671–1691. [[CrossRef](#)]
68. Mildon, Z.K.; Roberts, G.P.; Faure Walker, J.P.; Iezzi, F. Coulomb stress transfer and fault interaction over millennia on non-planar active normal faults: The Mw 6.5–5.0 seismic sequence of 2016–2017, central Italy. *Geophys. J. Int.* **2017**, *210*, 1206–1218. [[CrossRef](#)]

69. Papadopoulos, G.A.; Ganas, A.; Agalos, A.; Papageorgiou, A.; Triantafyllou, I.; Kontoes, C.; Papoutsis, I.; Diakogianni, G. Earthquake triggering inferred from rupture histories, DINSAR ground deformation and stress-transfer modelling: The case of central Italy during august 2016–January 2017. *Pure Appl. Geophys.* **2017**, *174*, 3689–3711. [[CrossRef](#)]
70. Picozzi, M.; Bindi, D.; Brondi, P.; Di Giacomo, D.; Parolai, S.; Zollo, A. Rapid determination of P wave-based energy magnitude: Insights on source parameter scaling of the 2016 central Italy earthquake sequence. *Geophys. Res. Lett.* **2017**, *44*, 4036–4045. [[CrossRef](#)]
71. Polcari, M.; Montuori, A.; Bignami, C.; Moro, M.; Stramondo, S.; Tolomei, C. Using multi-band insar data for detecting local deformation phenomena induced by the 2016–2017 central Italy seismic sequence. *Remote Sens. Environ.* **2017**, *201*, 234–242. [[CrossRef](#)]
72. Porreca, M.; Minelli, G.; Ercoli, M.; Brobia, A.; Mancinelli, P.; Cruciani, F.; Giorgetti, C.; Carboni, F.; Mirabella, F.; Cavinato, G.; et al. Seismic reflection profiles and subsurface geology of the area interested by the 2016–2017 earthquake sequence (central Italy). *Tectonics* **2018**, *37*, 1116–1137. [[CrossRef](#)]
73. Porreca, M.; Fabbri, A.; Azzaro, S.; Pucci, S.; Del Rio, L.; Pierantoni, P.P.; Giorgetti, C.; Roberts, G.; Barchi, M.R. 3D geological reconstruction of the M. Vettore seismogenic fault system (Central Apennines, Italy): Cross-cutting relationship with the M. Sibillini thrust. *J. Struct. Geol.* **2020**, *131*, 14. [[CrossRef](#)]
74. Ren, Y.; Wang, H.; Wen, R. Imprint of rupture directivity from ground motions of the 24 august 2016 Mw 6.2 central Italy earthquake. *Tectonics* **2017**, *36*, 3178–3191. [[CrossRef](#)]
75. Scognamiglio, L.; Tinti, E.; Casarotti, E.; Pucci, S.; Villani, F.; Cocco, M.; Magnoni, F.; Michelini, A.; Dreger, D. Complex fault geometry and rupture dynamics of the Mw 6.5, 30 October 2016, central Italy earthquake. *J. Geophys. Res. Solid Earth* **2018**, *123*, 2943–2964. [[CrossRef](#)]
76. Sextos, A.; De Risi, R.; Pagliaroli, A.; Foti, S.; Passeri, F.; Ausilio, E.; Cairo, R.; Capatti, M.C.; Chiabrande, F.; Chiaradonna, A.; et al. Local site effects and incremental damage of buildings during the 2016 central Italy earthquake sequence. *Earthq. Spectra* **2018**, *34*, 1639–1669. [[CrossRef](#)]
77. Smeraglia, L.; Billi, A.; Carminati, E.; Cavallo, A.; Doglioni, C. Field- to nano-scale evidence for weakening mechanisms along the fault of the 2016 Amatrice and Norcia earthquakes, Italy. *Tectonophysics* **2017**, *712–713*, 156–169. [[CrossRef](#)]
78. Stewart, J.P.; Zimmaro, P.; Lanzo, G.; Mazzoni, S.; Ausilio, E.; Aversa, S.; Bozzoni, F.; Cairo, R.; Capatti, M.C.; Castiglia, M.; et al. Reconnaissance of 2016 central Italy earthquake sequence. *Earthq. Spectra* **2018**, *34*, 1547–1555. [[CrossRef](#)]
79. Suteanu, C.; Liucci, L.; Melelli, L. The central Italy seismic sequence (2016): Spatial patterns and dynamic fingerprints. *Pure Appl. Geophys.* **2017**, *175*, 1–24. [[CrossRef](#)]
80. Testa, A.; Boncio, P.; Di Donato, M.; Mataloni, G.; Brozzetti, F.; Cirillo, D. Mapping the geology of the 2016 Central Italy earthquake fault (Mt. Vettore–Mt. Bove fault, Sibillini Mts.): Geological details on the Cupi–Ussita and Mt. Bove–Mt. Porche segments and overall pattern of coseismic surface faulting. *Geol. Field Trips Maps* **2019**. [[CrossRef](#)]
81. Tinti, E.; Scognamiglio, L.; Michelini, A.; Cocco, M. Slip heterogeneity and directivity of the ml 6.0, 2016, Amatrice earthquake estimated with rapid finite-fault inversion. *Geophys. Res. Lett.* **2016**, *43*, 10745–10752. [[CrossRef](#)]
82. Tung, S.; Masterlark, T. Delayed poroelastic triggering of the 2016 october visso earthquake by the august Amatrice earthquake, Italy. *Geophys. Res. Lett.* **2018**, *45*, 2221–2229. [[CrossRef](#)]
83. Tung, S.; Masterlark, T. Resolving source geometry of the 24 August 2016 Amatrice, central Italy, earthquake from insar data and 3d finite-element modeling. *Bull. Seismol. Soc. Am.* **2018**, *108*, 553–572. [[CrossRef](#)]
84. Valentini, A.; Pace, B.; Boncio, P.; Visini, F.; Pagliaroli, A.; Pergalani, F. Definition of seismic input from fault-based PSHA: Remarks after the 2016 central Italy earthquake sequence. *Tectonics* **2019**, *38*, 595–620. [[CrossRef](#)]
85. Valerio, E.; Tizzani, P.; Carminati, E.; Doglioni, C.; Pepe, S.; Petricca, P.; De Luca, C.; Bignami, C.; Solaro, G.; Castaldo, R.; et al. Ground deformation and source geometry of the 30 October 2016 Mw 6.5 Norcia earthquake (central Italy) investigated through seismological data, dinsar measurements, and numerical modelling. *Remote Sens.* **2018**, *10*, 1901. [[CrossRef](#)]
86. Walters, R.J.; Gregory, L.C.; Wedmore, L.N.J.; Craig, T.J.; McCaffrey, K.; Wilkinson, M.; Chen, J.; Li, Z.; Elliott, J.R.; Goodall, H.; et al. Dual control of fault intersections on stop-start rupture in the 2016 central Italy seismic sequence. *Earth Planet. Sci. Lett.* **2018**, *500*, 1–14. [[CrossRef](#)]

87. Wang, L.; Gao, H.; Feng, G.; Xu, W. Source parameters and triggering links of the earthquake sequence in central Italy from 2009 to 2016 analyzed with gps and insar data. *Tectonophysics* **2018**, *744*, 285–295. [[CrossRef](#)]
88. Whitney, R. Approximate recovery of residual displacement from the strong motion recordings of the 24 August 2016 Amatrice, Italy earthquake. *Bull. Earthq. Eng.* **2017**, *16*, 1847–1868. [[CrossRef](#)]
89. Wilkinson, M.W.; McCaffrey, K.J.W.; Jones, R.R.; Roberts, G.P.; Holdsworth, R.E.; Gregory, L.C.; Walters, R.J.; Wedmore, L.; Goodall, H.; Iezzi, F. Near-field fault slip of the 2016 Vettore Mw 6.6 earthquake (central Italy) measured using low-cost GNSS. *Sci. Rep.* **2017**, *7*, 4612. [[CrossRef](#)]
90. Xu, G.; Xu, C.; Wen, Y.; Jiang, G. Source parameters of the 2016–2017 central Italy earthquake sequence from the sentinel-1, alos-2 and gps data. *Remote Sens.* **2017**, *9*, 1182. [[CrossRef](#)]
91. Zimmaro, P.; Scasserra, G.; Stewart, J.P.; Kishida, T.; Tropeano, G.; Castiglia, M.; Pelekis, P. Strong ground motion characteristics from 2016 central Italy earthquake sequence. *Earthq. Spectra* **2018**, *34*, 1611–1637. [[CrossRef](#)]
92. Franke, K.W.; Lingwall, B.N.; Zimmaro, P.; Kayen, R.E.; Tommasi, P.; Chiabrando, F.; Santo, A. Phased reconnaissance approach to documenting landslides following the 2016 central Italy earthquakes. *Earthq. Spectra* **2018**, *34*, 1693–1719. [[CrossRef](#)]
93. Gori, S.; Falcucci, E.; Galadini, F.; Zimmaro, P.; Pizzi, A.; Kayen, R.E.; Lingwall, B.N.; Moro, M.; Saroli, M.; Fubelli, G.; et al. Surface Faulting Caused by the 2016 Central Italy Seismic Sequence: Field Mapping and LiDAR/UAV Imaging. *Earthq. Spectra* **2018**, *34*, 1585–1610. [[CrossRef](#)]
94. Pavlides, S.; Chatzipetros, A.; Papathanasiou, G.; Georgiadis, G.; Sboras, S.; Valkaniotis, S. Ground deformation and fault modeling of the 2016 sequence (24 August–30 October) in central Apennines (central Italy). *Bull. Geol. Soc. Greece* **2017**, *51*, 76. [[CrossRef](#)]
95. Perouse, E.; Benedetti, L.; Fleury, J.; Rizza, M.; Puliti, I.; Billant, J.; Woerd, J.V.d.; Feuillet, N.; Jacques, E.; Pace, B. Coseismic slip vectors of 24 August and 30 October 2016 earthquakes in Central Italy: Oblique slip and regional kinematic implications. *Tectonics* **2018**, *37*, 3760–3781. [[CrossRef](#)]
96. Tarquini, S.; Vinci, S.; Favalli, M.; Doumaz, F.; Fornaciai, A.; Nannipieri, L. Release of a 10-m-resolution DEM for the Italian territory: Comparison with global-coverage DEMs and anaglyph-mode exploration via the web. *Comput. Geosci.* **2012**, *38*, 168–170. [[CrossRef](#)]
97. Scarsella, F. La carta geologica d'Italia–scala 1:100.000. In *Foglio Geologico n. 132*; Foglio: Norcia, Italy, 1941; Available online: http://193.206.192.231/carta_geologica_italia/tavoletta.php?foglio=132 (accessed on 20 July 2020).



© 2020 by the author. Licensee MDPI, Basel, Switzerland. This article is an open access article distributed under the terms and conditions of the Creative Commons Attribution (CC BY) license (<http://creativecommons.org/licenses/by/4.0/>).